Taphonomic and diagenetic implications of reduction spot formation in Cretaceous red beds from the Jiaolai Basin, Eastern China

Fu, Wenzhao; Turner, Peter; Clements, Thomas; Spencer, Alan RT; Yu, Jifeng; Yang, Yu; Guo, Bangjie; Ning, Zhenguo; Zhuo, Zishun; Riley, Michael; Hilton, Jason

DOI:
10.1016/j.jseaes.2022.105533

Taphonomic and diagenetic implications of reduction spot formation in Cretaceous red beds from the Jiaolai Basin, NE China

Wenzhao Fu[a,*], Peter Turner[b], Thomas Clements[c], Alan R. T. Spencer[d,e], Jifeng Yu[f], Yu Yang[a], Bangjie Guo[g], Zhenguo Ning[h], Xizhun Zhuo[a], Michael S. Riley[c], Jason Hilton[c]

[a] Department of Geoscience and Engineering, College of Mining, Liaoning Technical University, Fuxin 123000, Liaoning, China

[b] 7 Carlton Croft, Streetly, West Midlands, B74 3JT, UK

[c] School of Geography, Earth and Environmental Sciences, University of Birmingham, Edgbaston, Birmingham, B15 2TT, UK

[d] Department of Earth Science and Engineering, Imperial College London, London SW7 2BP, UK

[e] Science Group, Natural History Museum, London, SW7 5BD

[f] Shandong University of Science and Technology, Qingdao 266590, Shandong, China

[g] National Key Laboratory of Remote Sensing Information and Image Analysis Technology, Beijing Research Institute of Uranium Geology, Beijing 100029, China

[h] Shandong Institute of Geological Survey, Jinan 250014, Shandong, China

* Corresponding author: Wenzhao Fu

E-mail address: fwzh04@163.com

Abstract

Green-grey coloured reduction spots are common in continental red beds through geological history and occur in a range of different lithologies and depositional environments, but their timing and mode of formation remain controversial. We investigate the Late Cretaceous to earliest Paleogene Jiaozhou Formation using borehole data from the Jiaolai Basin in Shandong province of northern China, and consider the distribution, morphology, and geochemistry of reduction spots in these continental red beds to evaluate how the reduction spots formed. Here, we report a novel application of three-dimensional X-ray Computed Tomography (XCT) to analyse reduction spot morphology, composition and density. Our data show that individual reduction spots are spheroidal, tubular or irregular shaped, and often contain small, grey, dark brown or black organic cores, referred to as loci. Typically, reduction spots have a similar chemical composition to the host red beds, but with elevated levels of vanadium (Va), lower levels of iron (Fe), and lower density. Isolated, small refractory fossils (e.g., charcoal) in the sediment alongside reduction spots but not within them indicates that microbial decay of organic labile (reactive) tissues in early diagenesis is an important control in reduction spot formation. We propose a new taphonomic model of reduction spot formation: post burial, during the primary sedimentary cycle in the groundwater zone, vanadium is released by intrastratal oxidation of titanomagnetite. Decay of organic matter creates localised reducing conditions resulting in the reduction of Fe^{3+} and the eventual depletion or removal of the resulting Fe^{2+} (altering the colour of the reduction spot).

Simultaneously, the reduction of V^{4+} and the consequent lowering of the concentration of V as V^{2+} minerals occur in the reduction spot, explaining their lower density than the host sediment.

Keywords: continental red beds; diagenesis, vanadium, redox, taphonomy, 3D X-ray Computed Tomography analysis

1. Introduction

Green-grey coloured reduction spots are common throughout geological history and have been observed stratigraphically from the Mesoproterozoic through the Phanerozoic (see Turner 1980; Hofman, 1991; Spinks et al., 2010; Table 1). Although they occur in various lithologies and depositional environments, their mode of formation remains controversial (Turner, 1980; Hofmann, 1991; Parnell, 1985, 1988; Parnell et al., 1987, 2016, 2018; Spinks, 2010, 2014). Hofmann (1991) summarised reduction 'spheroid' (referred to here as reduction spot) mineralogy and geochemistry across a range of stratigraphic contexts, and concluded that, despite the variation in age and lithology, reduction spots are similar in terms of their morphology, mineralogy, and geochemistry, potentially indicating a shared mode of formation. Typically, reduction spots cross-cut depositional laminations and bedding which, in combination with their shape and colour variations, suggest that they formed during diagenesis (Turner, 1980). However, the timing of formation is debated: the spheroidal nature of reduction spots has been used to suggest that they formed after sedimentary compaction, whilst vertically shortened examples may indicate growth prior to compaction (Spinks et al., 2010). Another feature of reduction spots is that many of them have a dark grey-black locus (or core), which has been inferred to be organic matter (OM) (Hofmann, 1990; Yang et al., 2019). Reduction spots tend to mimic the shape of the loci, suggesting a direct relationship between the development of a spot and its locus.

What triggers the formation of green-grey coloured reduction spots is contentious. Previously, it has been suggested that organic matter acts as a fuel source for microbial activity, and the decay of organic matter may have triggered localised reducing conditions around these loci points (e.g., Durrance et al. 1978; Turner 1980). However, Hofmann (1993) demonstrated that some reduction spot loci contained the mica roscoelite, which weathers to a dark brown colour (similar to that of organic matter), suggesting the possibility that some loci may not be organic rich. However, the absence of organics does not indicate that organics were never present; Hofmann (1990, 1993) concluded that microbial action was the most likely mode of reduction spot formation (see also Spinks et al., 2010) and that the absence of organic matter in some reduction spot loci could indicate simply that it had been fully consumed by microbial activity (Hofmann 1993).

The cause of the colour bleaching of reduction spots is primarily due to the absence of pigmentary iron oxide which gives the surrounding host sediment its red colour. Reduction spots and surrounding sediment contain a wide variety of minerals including roscoelite (V- mica), coffinite (U-silicate), cuprite (Cu-oxide), a variety of nickel (Ni), copper (Cu) and cobalt (Co) arsenides and sulphides, and a wide range of vanadate and uranyl vanadates (Hofmann, 1990; Chong et al., 2019). The origin of these minerals provides clues to the mechanisms of reduction spot formation. Many of these minerals are also present in large scale sedimentary hosted mineral deposits (Rose 1976; Brown et al 2014) for which leaching and transport of metals from host sediment with precipitation under changing redox conditions is a well-established mechanism. However, it is not clear if the formation of reduction spots and larger scale Uranium-vanadium (U-V) mineral deposition are part of a continuous process. Thorson (2004) and Hahn and Thorson (2005) suggested a two-stage process in which leaching occurred prior to a mineralization stage, while Asael et al. (2022) have shown the importance of redox controls at both local and regional scale using Copper (Cu) and lead (Pb) isotopes. These processes include the formation of reducing fluids by the alteration of organic material and the bleaching of formerly red sediments so that they are drab-coloured greens and greys (Barton et al 2018). Sufficiently reducing conditions would cause reduction of U^{6+} to U^{4+} and V^{4+} to V^{2+}; and in the reduced state these elements are less mobile, and mineralization can occur by combination with other elements. By contrast, the reduction of Fe^{3+} to the more mobile Fe^{2+} would result in the solution and removal of iron and subsequent bleaching of the reduced zone. It has been previously argued that diagenetic alteration of red beds can provide sufficient Cu for stratiform copper mineralization. The solubility of Cu is much increased in the presence of Cl^- rich solutions (Rose, 1976; Rose and Bianchi-Mosquera, 1993) and this could explain the common association of major bleached zones with evaporitic, arid climate deposits. The colour difference from the surrounding red sediment suggests *in-situ* reduction of ferric iron (Fe^{3+}) to ferrous iron (Fe^{2+}) and the dissolution and removal of pigmentary oxides (Sherlock, 1974). Cu^{+} in mineral deposits and reduction spots is frequently present as copper sulphide and in large scaled bleached zones the bacterial reduction of sulphate leached from associated evaporites is a likely mechanism of formation. The importance of faults in the migration of reducing fluids in bleached zones has been emphasised previously (Naylor et al. 1989) and described in more detail by Brown (2005).

Reduction spots are closely linked to the mechanism of formation of continental red beds and this is linked to palaeoclimate and the accumulation of organic material. In arid climates intrastratal alteration of non-red sediment (Walker et al., 1978) is dominant, but in humid, tropical climates partially reddened clay-rich alluvium is deposited. In the Late Triassic Newark Trough, Van Houten cycles recording lacustrine transgression and regression have colour variations ranging from black (perennial lake) to red (desiccated playa lake). These processional cycles result from the ~20kyr astronomical forcing cycle and now form the basis of the Late Triassic time scale (Olsen and Kent, 1996).

Within the continental red-beds of the Late Cretaceous-earliest Paleogene Jiaozhou Formation in the Jiaolai Basin, northeast China, gray-green reduction spots (typically with dark grey-black loci) are common making them an excellent case study for investigating the mode of reduction spot formation. Currently, the mode of reduction spot formation in the Jiaozhou Formation remains enigmatic (Yang et al., 2019). In this paper we evaluate the formation mechanism of reduction spots in the Jiaozhou Formation from the JK-1 borehole in Shandong Province and consider how this relates to their formation in other geological contexts. We achieve this by (i) reinterpreting the previoulsy identified depositional sedimentary environments by correlating the sediments of the JK-1 borehole with the nearby LK-1 borehole and interpreting lithological and faunal evidence, (ii) evaluating the physical and geochemical properties of the reduction spots and their host sediments, and (iii) proposing a new model for the formation of the reduction spots incorporating formation and eventual discoloration. We also (iv) propose a revised temporal framework for the lower part of the Jiaozhou Formation based upon a re-evaluation of a recently published cyclostratigraphic analysis (Yang et al., 2021), allowing us to consider the duration of its deposition and rates of change in sedimentary facies. Collectively, our data should help develop our understanding of the formation of reduction spots in continental red beds.

2. Geological background

The Jiaolai Basin is an Early Cretaceous composite rift basin with an area of approximately 12,000 km^2 in the Jiaozhou Peninsula of Shandong Province, northeast China (Fig. 1a, b). Formation of the Jiaolai Basin is related to subduction and retracement of the palaeo-Pacific plate into the Eurasian plate and the changing direction of their relative movement during the Mesozoic (Shen et al., 2020). Li and Hou (2018) identified three phases of stress field orientation during the Cretaceous evolution of the Jiaolai Basin, comprising NE-SW extension in the early Early Cretaceous, NNE-SSW extension in the later Early Cretaceous, and then E-W extension in the Late Cretaceous. The basin is bounded by the Jiaobei Terrane to the north, the NE trending Muping-Jimo Fault to the east, the NNE trending Tanlu Fault to the west (Fig. 1b, c), and the Sulu Ultra-High Pressure (UHP) metamorphic zone to the south (Zhang et al., 2003; Li, et al. 2020). The basin fill comprises Lower Cretaceous sediments of the Laiyang Group and igneous lithologies of the Qingshan Group, and the Late Cretaceous to early Paleocene Wangshi Group (Zhang et al., 2003; Tian et al., 2021). The Wangshi Group is dominated by purple to brick red conglomerate-sandstone-siltstone sets intercalated with marlstone from alluvial fan-fluvial-lacustrine facies, and also includes volcanic rocks. From the bottom to the top the Wangshi Group comprises the Linjiazhuang, Xingezhuang, Hongtuya, Shijiatun and Jiaozhou formations (Zhang et al., 2003; Tian et al., 2021). Zhang et al. (2021) inferred that the sediments of the Jiaozhaou Formation were provenanced from rocks in the Sulu UHP metamorphic zone to the south. Here we focus on the Shijiatun and Jiaozhou formations.

The Shijiatun Formation, comprising grey andesites in the lower part and black to greyish-brown basalts in the upper part, interbedded with red sandstones, siltstones and claystones, has been regarded by some authors to be the lowermost member of the Hongtuya Formation that occurred only locally in the Jiaozhou-Zhucheng area of the Jiaolai Basin (Ji, 2017; Tian et al., 2021). However, Ji (2017) and Li et al. (2020) considered it a separate formation restricted to the Jiaozhou-Zhucheng area based on its distinctive features. It comprises approximately 970 m of sedimentary and volcanic rocks that includes three separate eruptive phases intervened by two intervals of clastic deposition.

The Jiaozhou Formation is composed of purple, red, and pale green siltstones and claystones with occasional conglomerates and sandstones (Ji, 2017; Tian et al., 2021). Stratigraphically, the Jiaozhou Formation spans the K/Pg boundary, has been identified from gamma ray log (GR) profiles and anomalies in the concentration of the platinum group metal element, Iridium (Ir) (Xu, 2017). Based on this, Yang et al. (2021) used Gamma Ray log data from the JK-1 borehole (referred to in error as the ZK-1 borehole) to establish an astronomical timescale to determine the position of the K/Pg boundary. These studies demonstrate that continuous fluvial and lacustrine deposition occurred through the K/Pg boundary interval (Xu et al., 2019; Yang et al., 2021). The Jiaozhou Formation preserves a rich biota including charophytes, ostracods, and gastropods from shallow lacustrine settings, and sporopollen assemblages derived from terrestrial floras (Du et al., 2020; Li et al. 2020; Tian, et al. 2021; Yu et al. 2021). The charophyte flora of the Jiaozhou Formation have been analyzed biostratigraphically by Tian et al. (2021), and include typical Maastrichtian species (*Tolypella grambastii, Peckichara praecursoria, Microchara cristata, M. prolixa, Lamprothamnium ellipticum, Nodosochara* (*Turbochara*) *specialis,* and *Lychnothamnus* aff. *vectensis*) and Paleocene species (*Lychothamnus lanpingensis*), as well as species with ranges that span the boundary (*Chara changzhouensis*). The gastropod *Hydrobia datangensis* indicates a Late Cretaceous age, while the ostracod species *Porpocypris sphaeroidalis* indicates a Paleocene age (Yu et al., 2021).

Regarding palaeoenvironmental interpretations, Tan et al. (2019) suggested that the Jiaozhou Formation in LK-1 borehole (614–0 m) consists mainly of floodplain facies purple mudstones, grey-greenish siltstones and sandstones in the lower part (614–452 m), shore-shallow lacustrine, sage-green to purple mudstone in the middle part (452–250 m), and meandering fluvial, upward-thinning sandstones and mudstones with intercalated conglomerates and marlstones in the upper part (250–0 m). Subsequently, Li et al. (2020) divided the Jiaozhou Formation in the LK-1 borehole into seven intervals based primarily on lithological associations, in which the interval from 533–499 m is interpreted as shallow lake deposits, the interval from 498–426 m are channels and floodplain facies, while the interval of 425–311 m is returned to shallow lake deposits (Li et al., 2020, 2021; Yu et al., 2021). The other parts of the Jiaozhou Formation in the LK-1 borehole lack charophyte flora, which was interpreted to reflect climate cooling (Li et al., 2020, 2021). The K/Pg boundary transition charophyte flora of the Jiaolai Basin are composed of *Nodosochara* (*Turbochara*) *specialis*, which is characteristic of the deeper lacustrine facies, with seven other species, which inhabit mainly shallow lake facies. The Jiaolai Basin is considered to have developed as a high elevation intramontane palaeolake (Tian et al., 2021).

In the recently drilled JK-1 borehole, situated 1 km from the LK-1 borehole, reduction spots only occur in a 74 m thick interval at the bottom of the Jiaozhou Formation, situated between basalts of the Shijiatun Formation and green lacustrine mudstones that span the K/Pg boundary (Yu et al., 2021; Fig. 2). This 74 m interval comprises an alluvial-lacustrine continental red bed sequence (Tan et al., 2019; Li et al., 2020, 2021; Yu et al., 2021; Tian et al., 2021), but detailed sedimentological investigations and palaeoenvironmental interpretations of the JK-1 core, and precise correlation with the nearby LK-1 borehole, are yet to be undertaken. It is also unknown if diagenetic alteration of titanomagnetites from basalts from the Shijiatun Formation during the primary sedimentary cycle played a role in reduction spot formation as a source of vanadium in the Jiaozhou Formation. A more detailed sedimentological analysis involving the identification of transitional facies, like lacustrine shorefaces, can only be undertaken by consideration of surface outcrops and the 3D geometry of the facies (e.g., Deschamps et al. 2020). Such an analysis will be the focus of future research.

3. Materials and Methods

This study is based on analysis of the JK-1 borehole from Jiaozhou City in Shandong Province and its correlation to the LK-1 borehole that is approximately 1 km away. The JK-1 borehole (referred to as LX-1 by Yang et al., 2019) is located in the north of Dongxinzhi Village, Jiaozhou City (36°16′39″N; 119°58′06″ E) and was drilled by the Shandong Institute of Geological Survey. Borehole LK-1 is located to the west of Beixinzhi Village (36°15′57.98″N; 119°57′10.76″E) and was drilled by the Institute of Geology of the Chinese Academy of Geological Sciences and Shandong Institute of Geology in Jiaozhou (Li, Wang et al., 2016, 2020; Tian et al. 2021; Yu et al., 2021; Fig. 1).

Cores from the boreholes were logged, and lithology, grain size, sedimentary structures (along with a detailed log of the colour variations) were collected. Vertical profiles, coarse grain size, arrangement of facies and associated biota indicate that the sediments were deposited in an alluvial-fan lacustrine environment. The charophyte flora in LK-1 (Li et al., 2020) indicate the presence of shallow freshwater lakes and minor brackish ephemeral lakes associated with gypsum crusts and calcareous soils.

Reduction spots occur from 624–550 m in borehole JK-1 in brick red siltstone to fine sandstone. Samples were collected from 628 m, 624.8 m, 621.4 m, 611.1 m, 600 m, and 593.2 m depth and numbered *zk01* to *zk06* respectively. Of the samples, *zk01* to *zk04* did not contain reduction spots and had the suffix *r* added to denote their red colour, while *zk05* contained a few small reduction spots and also had the suffix *r* added to denote its dominantly red colour. Sample *zk06* was divided into two and re-labelled *zk06r* for red sediment and *zk06g* for the green part. In addition, 16 samples containing frequent reduction spots were photographed from 550.8 m to 599 m in the borehole core to analyze their physical features.

Samples with reduction spots were prepared by petrographic thin section before being observed under stereomicroscope and transmission polarizing microscopy in the Geological Lab Center at Liaoning Technical University (LNTU). Samples were powdered to 180 μm mesh to analyze clay mineral composition using X-ray diffraction, and to analyze major and trace elements using an Axiosm AX AB104L X-ray fluorescence spectrometer and NexION300D Plasma mass spectrometer. To determine loss on ignition values, individual samples were weighed then heated in crucible from 500℃ to 1000℃ for 60 mins and weighed again to determine loss. Using the results from the major elemental analysis, we calculated the Chemical Index of Alteration (CIA; Nesbitt and Young, 1982) and the Weathering Index of Parker (WIP; Parker, 1970) to quantitatively evaluate the weathering state of the investigated rock samples. The CIA is calculated as

$$Al_2O_3/(Al_2O_3 + CaO^* + Na_2O + K_2O) \times 100$$

while the WIP is expressed as

$$(2Na_2O/0.35 + MgO/0.9 + 2K_2O/0.25 + CaO^*/0.7) \times 100$$

CaO^* in the CIA refers to the calculated calcium content in the silicate fraction (McLennan et al., 1993).

Sample *zk06g* was scanned for Micro X-ray Computed Tomography (XCT) using a Zeiss Xradia 510 Versa at the Key Laboratory of the Institute of Geomechanics, Chinese Academy of Geological Sciences, Beijing. This method uses X-rays to collect 3D data of the sample's internal structure in which material density differences are reflected in the data by changes in X-ray attenuation. The scan was performed with 112 kV voltage, 112 µA current, and an exposure time of 1.5 s. No optical magnification was employed. The resultant 3D data attained a resolution of 22.01 µm per voxel (3D pixel). An image stack containing 1024 16-bit grayscale image slices, each 1024x1024px in size, was created. These were imported into a non-commercial version of Dragonfly (v2021.1; Object Research Systems (OSR) Inc.; https://www.theobjects.com/dragonfly/) for 3D volume rendering and analysis. In addition, a second 8-bit version of the dataset was generated with stretched brightness/contrast to aid the 3D surface rendering. First the datasets were cleaned by masking and removal of extraneous noise from outside the specimen. Then five regions of interest (ROIs) were selected and segmented by pixel thresholding of the 16-bit data, each representing a different material density range and visualised by a separate false colour. The false colours used are from (lower density) dark blue > light blue > yellow > red (higher density). Statistics from ten selected areas within the specimen were obtained, five from the red sediment and five from the reduction spot, using manually placed 1 mm^3 cube-shaped ROIs within the 16-bit data, for which minimum, maximum, mean, and standard deviation of the voxel values were calculated to determine density variations. Video animations of the 3D data were composed from Dragonfly generated images within the open-source software Blender (v3.1; The Blender Foundation; https://www.blender.org/).

Finally, samples *zk06r* and *zk06g* were broken into parts and the different coloured sediments were analyzed with a FEI Nova Nano SEM450 field emission scanning electron microscope (FE-SEM) at the Analysis and Testing Center of Beijing Research Institute of Uranium Geology. This analysis was to observe surficial features of the samples and to undertake geochemical analysis using the machine's Energy Dispersive Spectrometer (EDS) to identify the chemical composition at specific points.

4. Results and interpretation

4.1. Correlation of the LK-1 and JK1 boreholes and depositional facies

Sedimentary logs of JK-1 and LK-1boreholes are shown in Figure 2. Correlation between the boreholes is made from the position of the top of the stratigraphically youngest basalt (614 m in LK-1, 628 m in JK-1) which marks the boundary between the Shijiatun and Jiaozhou formations (Ding, 2016; Ji, 2017; Li et al., 2018; Wang et al., 2019; Han et al., 2020; Li et al., 2020). The depth of the K/Pg boundary has been identified from the Ir anomaly and GR profile at 523.35m in LK-1, and the GR profile at 537 m in JK-1 (Xu et al. 2017; Yang et al. 2021). After the volcanism of the Shijiatun Formation, the sedimentary succession commenced with a high energy alluvial fan facies that changed into lacustrine facies just below the K/Pg boundary. The two episodes of lacustrine facies are typified by mudstones and siltstones in the distal settings and sandstones in more proximal settings (Fig. 2).

Variations in the lithological features allow us to characterise the depositional environments further. Based on grain size trends and sandstone/mudstone ratios, there are clearly differences between the two boreholes. The lower part of the Jiaozhou Formation below the K/Pg boundary is similar in both the JK-1 and LK-1 boreholes. Similarly, the lacustrine interval which spans the K/Pg boundary is of similar thickness and shows a similar profile in both boreholes. Above the K/Pg boundary there are marked differences between the boreholes. In JK-1, the almost 50 m thick alluvial section from 517–463 m is very variable in grain size. The equivalent section in LK-1 from 500–448 m is coarser grained and less variable. Above this level the differences become accentuated even further: JK-1 is represented by finer grained sediments as lacustrine systems become dominant from 463–364 m, whereas in LK-1, coarse alluvial sediments dominate the section. Near the top of the profile (364–324 m in JK-1 and 351–310 m in LK-1) there is a return to more widespread lacustrine conditions. The lacustrine sections in JK-1 are in a more distal position within the depositional basin with finer grained sediments (Fig. 2).

4.2. Reduction spot morphology

In the JK-1 borehole, pale green reduction spots occur from 624–550m. Typically, these reduction spots have a dark grey, brown or black locus (or core) surrounded by a 'bleached' grey-green outer zone which contrasts sharply with the surrounding host red sediment. Figure 3 shows typical reduction spots including spheroidal (Fig. 3A, 3B), irregular (Fig. 3C–3F, 3H), and tubular (Fig. 3C, 3G, 3I) forms. The largest reduction spot in Figure 3C is irregular but has a tubular part with an elongated locus. In all cases where a locus is visible, the shape of the reduction spot exaggerates the overall shape of its locus, so the reduction spot appears to have developed around its locus. The irregular reduction spot shown in Figure 3C branches and has the appearance of a fossil plant axis or a palaeosol root. The other two reduction spots are tubular and have elongated loci; the overall reduction spot shapes exaggerate the shapes of their loci. Figure 3G shows vertical and near-vertical orientated tubular reduction spots that may represent 'rhizohalos' which formed around rhizoliths in palaeosols that developed on floodplains and around lake margins (Trendall et al., 2013). The reduction and removal of iron oxides around rhizoliths is widely reported in palaeosol studies (see Retallack, 2008; Kraus and Hasiotis, 2006). The spheroidal reduction spots illustrated in Figures 3A, B do not show visible loci but most likely formed around small fragments of organic material that was incorporated from plant communities on the floodplain and lake margins. It is possible that the loci in some reduction spots may not be visible because the plane of the image does not pass sufficiently close to the center of the spot.

Irregular and tubular forms typically have their long axes orientated parallel to bedding (Fig. 3C, 3I) and have smaller vertical extents suggesting they formed in early diagenesis prior to sedimentary compaction. In the JK-1 borehole, reduction spots range from 0.1 mm diameter spheroids (Fig. 3A; Table 2) to irregular bodies up to 65 x 40 mm (Fig. 3C–H; Table 2) in maximum dimension. Unlike larger reduction spots, the smallest ones of less than 0.5 x 0.5 mm diameter do not noticeably affect the overall red colour of the rock (Fig. 3C, 3E). In many of the reduction spots, the colour is slightly heterogenous with occasional small flecks of red less than 0.5 mm in diameter (Fig. 3D, 3E).

Reduction spots occur in red coloured mudstone, argillaceous siltstone, siltstone and fine sandstone (Table 2). Measurements taken come from two dimensional planes for which three-dimensional structure is more accurately characterised from X-CT results (see below). Maximum dimensions of reduction spots in mudstones are 22 x 20 mm (Fig. 4A; Table 2), while in argillaceous siltstone, siltstone and fine sandstone, there are abundant small ones less than 0.3 x 0.3 mm, while the largest are up to 60 x 40 mm in argillaceous siltstone, 65 x 25 mm in siltstone, and 50 x 40mm in fine sandstone (Fig. 4A; Table 2). Spherical reduction spots vary in size from 0.1–40 mm in diameter, while tubular ones from 6–65 mm and irregular ones from 3–50 mm in their maximum dimensions (Fig. 4B; Table 2); there is no consistent relationship of the reduction spot size to shape. Reduction spots with diameters of less than 10 x 10 mm consistently lack distinguishable loci, while larger reduction spots typically have distinguishable loci and occur in argillaceous siltstone, siltstone and fine sandstones (Fig. 4C; Table 2). There is no clear relationship between reduction spot size and how sharp or gradual their boundary is with the surrounding sediment other than those with largest diameters (>40 mm) have sharp rather than gradual boundaries (Fig. 4D; Table 2). Reduction spots with loci and a sharp boundary usually occur in very fine grained lithologies from mudstone and argillaceous siltstone (Fig. 4D), whereas reduction spots in sandstones more often contain gradual boundaries with the surrounding red sediment.

Petrographic images through the margin of a reduction spot in a red, fine-grained sandstone are shown in Figure 5A and 5B. Figure 5A shows a stereoscopic image of the very sharp boundary between the reduction spot and host sediment. In the drab area clear quartz grains are completely free of pigmentary iron oxides. The red host rock shows pigmentary grain coatings and the interstitial matrix is also stained red with fine grained iron oxides. Figure 5B shows a thin section photomicrograph of a reduction spot (left) and red host sediment (right). Red pigmentary oxides are interspersed in the matrix and there are also abundant opaque specularite grains that are probably oxidized titanomagnetite. Note that these opaque grains have a strong pigmentary grain coating. In contrast the reduction spot lacks abundant opaque minerals and pigmentary hematite. The sediment is arkosic with abundant feldspar overgrowths.

4.3. Fossil composition

In the JK-1 borehole from the 74m interval with reduction spots, plant fossils are typically from 1–7 mm wide and up to 50 mm long with sinuous rather than straight profiles and occasionally branch; these represent roots from palaeosols. Invertebrate fossils are extremely rare in this interval and, where present, are fragmentary, small (typically 1–3 mm) and often unidentifiable. Occasional fossils or fragments of fossil occur without reduction spots enveloping them, including shell fragments and the charcoal fragment shown in Figure 3I and 3J. These organic particles appear to have been inert during diagenesis and did not result in reduction spot formation around them. Variations in the nature of the organic matter in the sediment and its relationship to reduction spot formation is further considered below (see discussion).

4.4 Major and trace elements analysis

Major and trace element compositions of green reduction spots and the red host sediments are shown in Table 3 and Figure 6. The overall composition of the samples is very similar to that seen for sandstones in comparable tectonic settings (Middleton, 1960). There are only minor variations in major elements; the SiO_2 content ($\bar{x}$ = 52%) of siltstone and argillaceous siltstone samples numbered zk04 and zk05 is lower than that of fine sandstone samples zk02, zk03, zk06r and zk06g ($\bar{x}$ = 64%) (Fig. 6A, C). This is consistent with the fact that the finer grained lithologies are more poorly sorted and contain a higher proportion of clay minerals. Al_2O_3, Na_2O, K_2O, MnO, TiO_2, P_2O_5 and FeO contents of all samples show little difference (Fig. 6A, C). Sample zk05r contains much more CaO than any other samples, which suggests the siltstone to have a calcium carbonate cement, possibly of pedogenic origin (Fig. 6C).

Chemical Index of Alteration (CIA) values varies from 64.9–69.0 except for sample zk05r which is significantly lower at 37.0 (Table 3), while Weathering Index of Parker (WIP) values vary from 36.5–49.8. Both of CIA and WIP results show the siliclastic sediments in the source area have undergone moderate weathering.

The total iron content (Fe_2O_3) of the measured samples varies from 1.94 to 6.84% and the mean of red samples is 4.8%, a little higher than the overall average for red sandstones which is 1.7–3.5% according to Van Houten (1973). Typically, the amount of total iron increases with decreasing grain size and the average value of red mudstones is between 3.3–4.7%. The data presented here show a strong negative correlation between total iron and ferrous iron. The reason for this is unclear, but it maybe that grain size exerts a strong influence on iron composition.

Loss on ignition (LOI) values are shown in Table 3 and Figure 6A. Values range 6.65–14.93% ($\bar{x}$ = 9.42) and are relatively high. The lowest LOI values occur in sample zk06r (red sediment, 6.65%) and zk06g (green reduction spot, 6.66%), with other samples from the red sediments having significantly higher values than the reduction spots. LOI has been routinely used as a proxy for organic material in soil science (Jensen et al., 2018). These authors showed that the conventional conversion of soil organic carbon = 0.58LOI can be misleading, especially when the clay content is high, such that LOI values by themselves cannot be used to infer organic materials (OM) concentrations. The high values we record might be attributed to a higher clay (montmorillonite) content. The fact that the LOI values in zk06r and zk05g are similar would suggest similar organic carbon contents. Hofmann (1993) noted that the locus, reduction spot body sand host rock in a wide range of reduction spots had very low organic content (0.02% or less) but were always mineralised and characterised by the presence of roscoelite.

Comparison of trace elements (Fig. 6B, D) shows that each sample has nearly the same trace element composition except for the elements V, Sr, Ba and Zr, although there are small differences in Sr, Ba and Zr. However, the reduction spot sample *zk06g* has a concentration of up to 512 µg/g and contains almost five times the vanadium content of the other samples that have an average content of 77.56 µg/g. The average content of vanadium in the Earth's crust is approximately 135–140µg/g, while it is approximately 130 µg/g in shales and 20 µg/g in sandstones and carbonate rocks (Li, 1976; Mason and Moore, 1982; Tian and Zhang, 2016). Therefore, the vanadium content in the reduction spot sample *zk06g* is anomalously enriched. Vanadium enrichment in drab zones and reduction spots has been described by multiple authors (Turner, 1980; Hofmann, 1991).

4.5 X-ray diffraction analysis

Samples *zk03r*, *zk05r* and *zk06r* (red beds) and *zk06g* (reduction spot) were analyzed by X-ray diffraction to identify their mineral compositions to consider if there is a difference between the reduction spots and host red bed sediments (Fig. 8). Results indicate similar mineral compositions in the host red sediment and reduction spots, comprising quartz, feldspar, mica, montmorillonite, maghemite and harmotome.

The overall mineral composition of the Jiaozhou Formation is comparable to many other continental red beds, especially those composed of first cycle alluvium (Suttner and Dutta, 1986) with quartz, feldspar and mica, the main framework constituents. The iron oxide maghemite (oxidized titanomagnetite) and the barium zeolite mineral harmotome may represent minor detrital components derived from the intercalated basalts; harmotome is normally associated with higher temperatures and is most commonly found in basaltic rocks. The swelling clay montmorillonite forms as a result of intrastratal alteration of feldspars and ferromagnesian silicates (Walker, 1976; 1978) and represents cements formed during diagenesis. During burial montmorillonite is transformed into illite (Pytte and Reynolds, 1989). This transition has widely been used as a geothermomenter (Pollastro, 1993) with the onset of transition starting at about 100°C closely coincident with the start of petroleum generation. The XRD results indicate that montmorillonite (smectite) is the dominant clay mineral. On this basis we conclude that the rocks have not been deeply buried or subjected to petroleum generation. Although we are not able to identify the mineral from whole rock XRD data, the data do show a small peak at 9° 2θ which would correspond to the 001 reflection of roscoelite (Fig. 8).

4.6 3D X-ray Computed Tomography (XCT)

Sample *zk06g* including a spherical reduction spot with dark locus in red sediment was observed under 3D XCT to analyse three-dimensions density variations in its internal structure. Results from the XCT data surface rendering (Fig. 9A–C), relative density false colour segmentation (Fig. 9D–F) and combination of the surface rendering and false colour segmentation (Fig. 9G–I) all enable the boundary of the reduction spot to be distinguished from the surrounding sediment. The CT rendering (Fig. 9A–C) allows the external surface of the specimen to be visualised, with the reduction spot visible as a darker zone compared to the surround red sediment. This distinction is more visible in the false colored segmentations (Fig. 9D–F), where discrete ranges of different relative density material, from lower to higher density, are shown as: dark blue > light blue > green > yellow > orange > red. The sharp boundary of the reduction spot can be readily identified from the false colour images due to its general relative low-density reflected by its overall blue colour, whereas the surrounding sediment has an overall orange colour (Fig. 9 D–F) depicting relative higher-density composition. The reduction spot also has a lower frequency of relative high-density contents compared to the surrounding sediment, and these are typically of smaller size (Fig. 9D–F). The combined CT rendering and false colour overlays (Fig. 9G–I) show the same as the separate lines of evidence but make it easier to identify the position individual minerals on the surface of the specimen.

Analysis of the ten manually placed regions of interest in the sample show the mean 16-bit grayscale pixel value, which equate to relative density. For the five values from the reduction spot this is 8359.9, whereas the mean of the five values attained from the red sediment is approximately 4.1% higher at 8704.8 (Table 4).

Small, irregular and high-density features occur throughout the sample in both red sediment and reduction spots, but this method does not permit their composition to be identified with certainty. The high-density objects shown in red in the false colour model may represent metallic-rich minerals of detrital origin or organic tissues that have decayed and been mineralized by vanadium or other transition metals. The relative mid-density features in orange are smaller and appear much more frequent in the red sediment than within the reduction spot.

4.7 Energy Dispersive Spectrometry (EDS)

The positions of Energy Dispersive Spectrometer (EDS) point analyses are shown in Figure 10 and the corresponding results in Table 5. Samples P7, P10 and P11 (Table 5) are from the reduction spot loci whilst P17, P18 and P19 are from green reduction spot bodies. Two of the sample points P3 and P5 show higher proportions of iron (78.7–79.8%) and chromium (17.5–18.1%), possibly indicating the presence of chromite ($FeCr_2O_4$), most likely of detrital origin.

The composition of samples from the reduction spot loci and bodies are broadly similar with only minor differences between silica, magnesium, sodium, and calcium (Table 4). There are however important differences between potassium (0.85% vs 1.51%), aluminium (10.63% vs 8.44%), iron (0.85% vs 1.17%) and vanadium (0 vs

1.51%) (spots P3 and P5 are excluded from the mean calculation). These data lend further support to the idea of redistribution of elements during reduction spot formation. It suggests to us that whilst vanadium was originally sequestered by organic material in the loci of the reduction spot, as the organic material was metabolized V was released back into the system along with other elements including potassium and iron. During subsequent diagenesis it may well have been incorporated into other inorganic minerals. Although not identified in our XRD data, probably because of limitations on the detection limits, it seems likely that the V may be present in the reduction spots as roscoelite ($K (V^{3+}, Al.Mg)_2 AlSi_3O_{10} (OH)_2$).

5. Discussion

5.1. Palaeoenvironment of red beds in the Jiaozhou Formation

Based on charophyte distributions in the Jiaozhou Formation, Li et al. (2020) thought most of the water bodies were freshwater lakes, although there was evidence for subordinate brackish water conditions. The occurrence of gypsum crusts and calcareous palaeosols in LK-1 is consistent with this interpretation (Li et al., 2020).

Our data indicate that the late Cretaceous red beds of the Jiaozhou Formation formed in a humid, warm, oxic, continental freshwater environment; most likely an alluvial-fan lacustrine environment. Below we consider the evidence for this interpretation. The colour of modern alluvial sediments in humid tropical climates has been described in detail by van Houten (1973) and Walker (1974). They are mainly greyish brown, brown or yellowish brown in colour and contain abundant hydrated iron oxides. Colour variations are noted relating to the degree of pedogenesis on alluvial floodplains. The red colouration is produced by the aging of hydrated iron oxides and the formation of hematite during diagenesis and pedogenesis. The late Cretaceous red beds of the Jiaozhou Formation comprise first cycle detritus supplied by the high-grade metamorphic rocks and Cretaceous igneous lithologies of the Sulu Orogen and the basic igneous lithologies underlying the formation. Furthermore, the influx of terrigenous sediment also introduced allochthonous labile and refractory OM (discussed below). The presence of occasional gypsum crystals indicates periods of periodic evaporation, in which plants colonized the sediment, developing root complexes, and eventually calcareous palaeosols. Continued high sedimentation rates would have led to these palaeosols becoming inundated in turn.

The sandstones show dissolution and alteration of feldspars and ferromagnesian silicates with the precipitation of authigenic quartz, clay minerals, feldspars and iron oxides. The presence of finely crystalline hematite on detrital grains is consistent with a diagenetic origin of the red colour (Walker, 1967, 1974, Turner, 1980), however, we cannot rule out the presence of detrital ferric hydroxides. The clear implication is that the sediment was non-red at the time of deposition and has become red during burial and diagenesis.

Sr/Ba and Fe/Mn ratios and MnO_2 content can reflect the palaeosalinity of sedimentary environment (Liu, 1980). All the samples from the JK-1 core have Sr/Ba <0.6, Fe/Mn >5, and the average content of MnO_2 is 0.00052 indicating that the clastic rocks formed in continental freshwater sedimentary environments (e.g. Turner, 1980).

The ratios of Cu/Zn, (Cu+Mo)/Zn, and Sr/Cu can indicate redox conditions in sedimentary environments (Hallberg et al., 1976). In the JK-1 borehole, the red beds formed in an oxidizing environment with high temperature because the ratio value of Cu/Zn and (Cu+Mo)/Zn were less <1 and value of Sr/Cu were close to and slightly higher than 10.

Quality fraction of oxides and the corresponding ratio of K_2O/Na_2O plotted against SiO_2/Al_2O_3 (Fig. 7a) shows that samples from the JK-1 borehole formed in an active continental margin setting (Roser and Korsch, 1986). Composition of the trace elements La, Th and SC in sandstone, plotted in a ternary diagram (Fig. 7b), shows that red beds have composition similar to those from active continental margins settings and formed related to volcanism (Mao and Liu, 2011; Tian and Zhang, 2016; Fig. 7b).

5.2. Origin and nature of organic matter in the Jiaozhou Formation

In the Jiaozhou Formation, organic matter (OM) is abundant and derived from organisms living in the alluvial to lacustrine environments including terrestrial and aquatic plants, wind- and water-borne pollen and spores, invertebrate and vertebrates. In the JK-1 core, the OM comprises fine-grained, amorphous particles that have been reworked and distributed by sedimentary processes, and larger (mm-cm diameter) carbonaceous plant axes and roots from palaeosols, as well as occasional charcoalified plant matter. From the LK-1 borehole Li et al. (2020) and Tian et al. (2021)

documented charophyte and gastropod assemblages, with charophytes restricted to aquatic environments while gastropods are vagrant and can live in water and damp terrestrial conditions. In the JK-1 borehole, reduction spots formed over a relatively narrow stratigraphic interval in the basal 74 m of the Jiaozhou Formation spanning an estimated duration of 0.45 Ma (Fig. 2). During this interval, palaeosol development indicates a hiatus in sedimentation for plants to grow, increasing the concentration of OM as rootlets and litter.

The survival of plant matter in the Jiazhou Formation is unsurprising but it only occurs within reduction spots. Plant tissues, especially those that provide structural support (i.e. contain cross-linked macro molecules such as lignin) may be taphonomically recalcitrant and geologically stabilized during diagenesis (Briggs, 1999). Similarly, as products of wildfire, charcoalified plant tissues (= the coal maceral inertinte) are refractory and do not undergo decay post-mortem during burial and early diagenesis due to high carbon content (e.g., Scott, 2010). However, non-plant OM in the Jiaozhou Formation is often difficult to identify, most likely due to the taphonomic processes that occurred pre and post burial. Labile organic components (e.g. non-biomineralised, soft tissues such as skin, internal organs, hair, feathers) rapidly undergo post-mortem decay from microbial activity either before or during burial or early diagenesis (e.g., Brenchley and Harper, 1998; Tyson, 1995). In contrast, refractory organic components comprising organic hard parts containing collagen and inorganic minerals, including calcium phosphate (e.g., vertebrate bones, teeth, scales), calcite, or aragonite (e.g., mollusc shells) are more recalcitrant, decaying at a slower rate (Brenchley and Harper, 1998, Tyson, 1995). The principal abiotic process of collagen breakdown is hydrolysis, which may occur alongside microbial degradation. Demarchi et al. (2016) identify the major control on collagen preservation in porous minerals to be the surface binding of the component collagen peptides to the mineral skeleton, which stabilizes both the peptides and the water in contact with them. They suggest that collagen under these conditions may remain substantially intact for millennia. Consequently, the release of collagen from refractory organics due to hydrolysis is extremely slow, which suggests that the concentrations of organic material produced abiotically from a refractory organic would be unlikely to build up sufficiently to generate reduction spot loci, which is consistent with the absence of refractory organics in the reduction spots seen in our data. Acidic burial conditions and microbial metabolism will cause mineral dissolution and exacerbate the speed of collagen break down (Collins *et al.* 1995, 2003; Collins and Riley, 2000). The abiotic breakdown of collagen is also temperature dependent, with degradation rates increasing at higher temperatures (Collins *et al.* 1995) and higher temperatures also increase the rate of degradation due to microbial action (Briggs and Kear 1993b). The breakdown of organics by microbial action would alter the geochemistry of the surrounding sediment and would be the potential trigger/driver to the formation of reduction spots. A potential model for the formation of these reduction spots is discussed below.

5.3. Source of vanadium

The origin of vanadium is unknown but is likely to have been derived from the underlying basic igneous lithologies either through the weathering and its absorption into groundwater, or as detrital grains in the first alluvial cycle. It is likely to have been ubiquitous in the interstitial water through the sediment but in very low concentrations as suggested by its low concentration in the sedimentary red beds (Tables 3, 4). Vanadium is concentrated and precipitated in reduction spots as outlined below.

5.4. Model for reduction spot formation in the Jiaozhou Formation

A model showing the formation of the reduction spots is shown in Figure 11. After burial, labile OM decays in the sediment under aerobic conditions (Stage 1 in Figure 11). Microbial metabolism of labile tissues would use, and deplete, the available free oxygen from porewater, while increasing levels of waste bi-products including CO_2 (aq), H_2SO_4, as well as liberating organic ligands from the OM, such as fatty acids, (see Briggs and Kear, 1993a, 1993b). The release of these metabolic bi-products would alter the geochemical conditions directly around the OM, creating localised microenvironments that were oxygen depleted, acidic, and increasingly reducing (e.g. Sagemann et al. 1999; Raiswell and Fisher 2000) (Stage 2 in Figure 11). At this stage the microbial communities would begin to use iron oxides as a respirant and the migration of released iron would be set in place. Lentini et al. (2012) have shown that iron-reducing bacterial communities are influenced by the oxide mineralogy and the nature of the carbon substrate. The hydrated oxides ferrihydrite and goethite are more reactive than hematite. Lentini et al. (2012) showed that only ferrihydrite was reduced in the presence of acetate, but when glucose and lactate were available goethite and hematite were also reduced. This change coincided with the presence of *Desulfobrivio* spp. and *Enterobacter* spp. indicating the presence of sulphate reduction and fermentation processes. Information on the range of microbial groups and their activity with different carbon sources is described by Su et al. (2020). As OM consisting of labile tissues was the fuel source for the microbial metabolism, these OM would have, therefore, acted as the locus points for these geochemically distinct microenvironments that typically would have expanded isotropically by molecular diffusion (Stages 3 and 4 in Figure 11). This explains the typical spherical nature of many of the reduction spots observed surrounding smaller fragments of OM. Around larger OM fragments (e.g., plant roots), the reduction spots are larger and often mimic the morphology of the OM – adding further evidence that the OM acted as a fuel source for the generation of microbial-induced microenvironments. In the Jiaozhou Formation, fossil plant remains are only found in association with reduction spots. Conversely, we do not observe reduction spots around refractory OM such as charcoalified plant matter (fusinite) or non-labile shell material, further strengthening the hypothesis that the microbial metabolism of labile tissues drove the generation of reducing microenvironments within the sediment.

Sediment porosity would have been a key factor in limiting the diffusion of decay products away from the OM (see McCoy et al. 2015). In the Jiaozhou Formation we observe that the boundary of the reduction spot is diffuse in the coarser-grained fine sandstones, whereas the boundaries of these redox zones are much sharper in mud and silt dominated sediments. The spherical nature of many reduction spots suggests that there was little or no flow in the groundwater during their formation; asymmetry or diffusion (and eventually obliteration of the microenvironment) might be envisaged along the primary flow direction if present. In our analysis, irregular shaped reduction spots only developed around irregular shaped fossil plant loci, with reduction spot margins developing uniformly around these irregular shapes.

Once the available oxygen in porewater has been consumed, bacterial populations within the sediment would be forced to utilise other oxidants during the breakdown of OM (Allison, 1988). In terrigenous sediment with ample supply of Fe, it is highly likely that within the localised anerobic reduction zone, Fe was utilised by the bacteria as an electron acceptor. Furthermore, it is possible that as the iron oxides are reduced, the Fe^{2+} is more mobile and may have diffused away from the reduction spot further depleting the microenvironment around the OM. This would explain the lower relative density of the reduction spots in relation to the surrounding red beds which would have higher proportions of dense pigmentary iron oxides including hematite (see XCT results).

As the pore water becomes more reduced, the vanadium and is fixed in association with the OM and changes valency from V^{4+} to V^{2+}. It should be noted that anerobic bacteria often show anerobic plasticity, and that some species of vanadium reducing bacteria have been identified (Myers *et al.* 2004). This results in a reduction spot with elevated V concentrations compared to the host sediment. The form in which the V is present is not known; we have not identified any of the common V-bearing minerals such as roscoelite.

The microenvironments around the OM would have been sustained until the OM fuel source was exhausted — as can be potentially identified by our LOI values but agreeing with the low OM concentrations in reduction spots reported by Hofmann (1993), or until conditions became unfavorable for bacterial activity to continue. Our observations of smaller reduction spots without OM loci could represent an exhausted fuel source.

Finally, as the sediment became buried, compacted, and moved into early diagenesis, the localised sediment surrounding OM became green due to the removal of Fe and the fixation of V and U, while the main sedimentary matrix became red as iron oxide precipitated. Where reduction spots have very sharp boundaries (e.g., Fig. 5A–C) it indicates the maximum extent or outer limit of the removal of pigmentary iron oxides. The fate of the iron removed in this way is not clear, but it is plausible that it has been used as a metabolic agent for anerobic bacterial metabolism (Berner, 1981; Allison, 1988). It would depend on the chemical conditions of the reducing fluid, not least the presence of Cl^- which would increase the solubility of iron. Iron oxide would be reprecipitated as soon as oxidizing conditions return, for example as small Fe-Mn nodules as seen in some Triassic palaeosols (Trendall et al., 2013), or it could become incorporated into other authigenic minerals which might be forming at the same time e.g. as newly formed pigmentary hematite.

6. Conclusions

(1) The palaeoenvironement of the latest Cretaceous continental red beds from the basal part of the Jiaozhou Formation in the Jiaolai Basin, North China, is reinterpreted as high energy alluvial fan and fan delta facies that changed into lacustrine facies just below the K/Pg boundary.

(2) In the Jiaozhou Formation, reduction spots formed in the first alluvial cycle around fossil plant tissues in palaeosols during early diagenesis. The geochemical data from reduction spots is consistent with the migration of Fe^{2+} from the reduction spot into the surrounding sediment. Subsequent oxidation would likely enhance its red colouration. Vanadium is strongly enriched in the reduction spot loci due to incorporation of VO^{2+} in organic compounds, thereby contributing to the dark colour of the reduction spot loci .

(3) In the past there has been disagreement on how continental red beds became red, with different studies suggesting it was either from incorporation of oxidized, reddened alluvial sediments, or through *in*-situ intrastratal alteration during diagenesis. In the Jiaolai Basin the sharp colour contrast between the grey-green lacustrine and red alluvial sediment shows that there was an important depositional control. Our observations of intrastratal oxidation of silicates and titanomagnetites shows that both processes were operative and provided a complex environment in which the reduction spots formed.

(4) X-CT analysis reveals reduction spots have a lower relative density, presumably resulting from the migration of Fe from the reduction spot to the

surrounding sediment where it deposited as thin coatings of pigmentary iron oxides on mineral grain surfaces during diagenesis.

(5) We develop a four-stage taphonomic model for the formation of reduction spots in the Jiaozhou Formation. Microbial metabolism of labile fossil components generated localized geochemical conditions that reduced Fe^{3+} into the more mobile Fe^{2+}, which would be depleted or removed via continued metabolism or diffusion, while simultaneously the reduction of V^{4+} to V^{2+} reduced the density of the reduction spots. This process would also change the colour of the spots into the grey-green hue. Meanwhile refractory fossils within the sediment, such as charcoal, could not be utilized by microbial activity, which explains why these fossils do not act as loci for the reduction spots.

Acknowledgments

This research was financially supported by the Liaoning Provincial Department of Education Youth Foundation (Grants LJ2017QL027), China Scholarship Council State Scholarship Fund (Grant 201908210471), Shandong Provincial Key Laboratory of Depositional Mineralization and Sedimentary Minerals Opening Foundation (Grants DMSM201405), Shandong Geological Prospecting Project (Grant Lukan2021-1), and National Science Foundation of China (Grant 41472092). TC is funded by a Leverhulme Early Career Fellowship (ECF-2019-097). We thank Engineers Kemin XU and Zhigang ZHANG (Shandong Institute of Geological Survey) for sampling assistance, Junhu WANG (Beijing Research Institute of

Uranium Geology) and Shengxin LIU (Key Laboratory of the Institute of Geomechanics, Chinese Academy of Geological Sciences) for sample analysis assistance. This manuscript was improved by editorial recommendations from A. E. Radwan and MeiFu Zhou, and two anonymous reviews.

References

Allison, P. A. 1988. Konservat-Lagerstätten: cause and classification. Paleobiology, 14(4): 331–344.

Asael, D., Matthews, A., Bar-Matthews, M., Harlavan, Y., Segal, I., 2012. Tracing redox controls and sources of sedimentary mineralization using copper and lead isotopes. Chemical Geology, 310: 23–35.

Barton, I., Barton, M.D., Thorson, J., 2018. Characteristics of Cu and UV deposits in the Paradox Basin (Colorado Plateau) and associated alteration. Society of Economic Geologists, Guidebook series, 59: 73–102.

Benton M.J., Gray D.I., 1981. Lower Silurian distal shelf storm-induced turbidites in the Welsh Borders: sediments, tool marks and trace fossils. Journal of the Geological Society, 138: 675–694. https://doi.org/10.1144/gsjgs.138.6.0675

Berner, R.A. 1981. Authigenic mineral formation resulting from organic matter decomposition in modern sediments. Fortschritteder Mineralogie, 59: 117–135.

Beutner, E.C., Charles, E.G., 1985. Large volume loss during cleavage formation, Hamburg sequence, Pennsylvania. Geology, 13(11): 803–805.

Brenchley, P.J., Harper, D.A.T., 1998. Palaeoecology: Ecosystems, Environments and

Evolution. Chapman and Hall: London. 402 pgs.

Briggs, D.EG. 1999. Molecular taphonomy of animal and plant cuticles: selective preservation and diagenesis. Philosophical Transactions of the Royal Society of London B, 354(1379): 7–17.

Briggs, D.E., Kear, A.J. 1993a. Fossilization of soft tissue in the laboratory. Science, 259(5100): 1439–1442.

Briggs, D.E., Kear, A.J. 1993b. Decay and preservation of polychaetes: taphonomic thresholds in soft-bodied organisms. Paleobiology, 19(1), 107–135.

Brown, A.C., 2005. Refinements for footwall red-bed diagenesis in the sediment-hosted stratiform copper deposits model. Economic Geology, 100(4): 765–771.

Brown, A.C., Turekian, K., Holland, H., 2014. Low-temperature sediment-hosted copper deposits. Treatise on Geochemistry, 13: 251–271.

Chong, S., Aksenov, S.M., Dal Bo, F., Perry, S.N., Dimakopoulou, F., Burns, P.C., 2019. Framework polymorphism and modular crystal structures of uranyl vanadates of divalent cations: Synthesis and characterization of $M(UO_2)(V_2O_7)$ (M = Ca, Sr) and $Sr_3(UO_2)(V_2O_7)$ 2. Zeitschrift für Anorganische und Allgemeine Chemie, *645*(15): 981–987.

Collins, M.J., Riley, M.S. 2000. Amino acid racemizaion in biominerals, the impact of protein degradation and loss. Pages 120–142 in Goodfriend, G., Collins, M.J., Fogel, M., Macko, S., Wehmiller, J. (Eds). Perspectives in Amino Acid and Protein Geochemistry. Oxford University Press, New York.

Collins, M.J., Riley, M.S., Child, A.M., Turner-Walker, G. 1995. A basic mathematical simulation of the chemical degradation of ancient collage. Journal of Archaeological Science, 22: 175–183.

Collins, M.J., Walton, D., Curry, G.B., Riley, M. S., Von Wallmenich, T.N., Savage, N.M., Muyzer, G., Westbroek, P. 2003. Long-term trends in the survival of immunological epitopes entombed in fossil brachiopod skeletons. Organic Geochemistry, 34: 89–96.

Demarchi, B., Hall, S., Roncal-Herrero, T., Freeman, C.L., Woolley, J, Crisp, M.K., Wilson, J., Fotakis, A., Fischer, R. ,Kessler, B.M., Jersie-Christensen, R., Olsen, J. V., Haile, J., Thomas, J., Marean, C.W., Parkington, J., Presslee, S., Lee-Thorp, J., Ditchfield, P., Hamilton, J.F., Ward, M.W., Wang, C.M., Shaw, M.D., Harrison, T., Dominguez-Rodrigo, M., DE MacPhee, R., Kwekason, A., Ecker, M., Horwitz, L.K., Chazan, M., Kroeger, R., Thomas-Oates, J., Harding, J.H., Cappellini, E., Penkman, K., Collins, M. J. 2016. Protein sequences bound to mineral surfaces persist into deep time. eLife, 5: e17092.

Deschamps, R., Dohais, S., Hamon, Y., Gasparrini, M., 2020. Dynamic of a lacustrine sedimentary system during late rifting at the Cretaceous-Paleocene transition: Example of the Yaxoraite Formation, Salta Basin, Argentina. The Depositional Record, 6 (3): 490–523. https://doi.org/10.1002/dep2.116

Ding, C., 2016. The ostracod biostratigraphy and the K/Pg boundary discussion in LK1 core, Jiaolai Basin, Master's degree Thesis, China University of Geosciences (Beijing): 1–65 (in Chinese with English language abstract).

Du, S., Chen, J., Chen, C., Gao, L., Liu, F., Song, X., Tian, J., Zhang, S., Liu, S.,

2020. Biostratigraphy of the Jiaozhou Formation in the Jiaolai Basin, Shandong, eastern China, with discussion of the Cretaceous-Paleogene Boundary. Journal of Stratigraphy, 44(1): 22–34 (in Chinese with English language abstract).

Durrance, E.M., Meads, R.E., Ballard R.R.B., Walsh J.N., 1978. Oxidation state of iron in the Littleham Mudstone Formation of the New Red Sandstone Series (Permian-Triassic) of Southeast Devon, England Geological Society of America Bulletin, 89: 1231–1240. https://doi.org/10.1130/0016-7606(1978)89<1231:OSOIIT>2.0.CO;2

Guo, X., Retallack, G.J., Lü, B., He, L., Wang, R. Song, H., 2019. Paleosols in Devonian red-beds from northwest China and their paleoclimatic characteristics. Sedimentary Geology, 379: 16–24. https://doi.org/10.1016/j.sedgeo.2018.11.001.

Hahn, G., Thorson, J., 2005. Geology of the Lisbon Valley sandstone-hosted disseminated copper deposits, San Juan County, Utah, *in* Gloyn, R., Park, G., Spangler, L., eds., Utah Geological Association Publication 32: 19–42.

Hallberg, J.A., Johnston, C., Bye, S.M., 1976. The Archaean Marda igneous complex, Western Australia. Precambrian Research, 3(2):111–136

Han, F., Sun, J., Qin, H., Wang, H., Ji, Q., He, H., Deng, C. Pan, Y., 2020. Magnetostratigraphy of the Upper Cretaceous and Lower Paleocene terrestrial sequence, Jiaolai Basin, eastern China. Palaeogeography, Palaeoclimatology, Palaeoecology, 538: 1–12. https://doi.org/10.1016/j.palaeo.2019.109451.

Harrison, R.M., Pio, C.A., 1983. Major ion composition and chemical associations of inorganic atmospheric aerosols. Environmental Science Technology, 17: 169–

174.

Hofmann, B.A. 1990. Reduction spheroids from northern Switzerland: Mineralogy, geochemistry and genetic models. Chemical Geology, 81: 55–81. https://doi.org/10.1016/0009-2541(90)90039-A.

Hofmann, B.A. 1991. Mineralogy and geochemistry of reduction spheroids in red beds. Mineralogy and Petrology, 44(1–2): 107–124.

Hofmann, B.A. 1993. Organic matter associated with mineralized reduction spots in red beds. Bitumens in Ore Deposits, 9: 362–378. 10.1007/978-3-642-85806-2_19.

Jensen, J.L., Christensen, B.T., Schjønning, P., Watts, C.W. and Munkholm, L.J., 2018. Converting loss-on-ignition to organic carbon content in arable topsoil: pitfalls and proposed procedure. European Journal of Soil Science, 69(4): 604–612.

Ji, Q., 2017. On the Cretaceous stratigraphic framework and the Cretaceous-Paleogene boundary of eastern Shandong province. Journal of Geology, 41(1): 1–25 (in Chinese with English language abstract).

Kraus, M.J., Hasiotis, S.T. 2006. Significance of different modes of rhizolith preservation to interpreting paleoenvironmental and paleohydrologic settings: examples from Paleogene paleosols, Bighorn Basin, Wyoming, USA. Journal of Sedimentary Research 76(4): 633–646. https://doi.org/10.2110/jsr.2006.052

Lentini, C.J., Wankel, S.D., Hansel, C.M., 2012. Enriched iron (III)-reducing bacterial communities are shaped by carbon substrate and iron oxide mineralogy. Frontiers in Microbiology, 3: Art. 404. https://doi.org/10.3389/fmicb.2012.00404

Li J., Hou, G. 2018. Cretaceous stress field evolution and origin of the Jiaolai Basin, Eastern North China. Journal of Asian Earth Sciences, 160: 258–270.

Li, S., Wang, Q., Zhang, H., Wang, H., Wan, X., 2020. Latest Campanian to Maastrichtian charophytes in the Jiaolai Basin (Eastern China). Cretaceous Research, 106: 1–15.https://doi.org/10.1016/j.cretres.2019.104266.

Li, T. 1976. Chemical element abundances in the earth and it's major shells. Geochimica, 3: 167–174. (in Chinese with English language abstract)

Mao, G., Liu, C., 2011. Application of geochemistry in provenance and sedimentary background analysis. Journal of Earth Sciences and Environment, 33(04): 337–348 (in Chinese with English language summary).

Mason, B., Moore, C.B. 1982. Principles of Geochemistry (Four Edition). New York: John Wiley & Sons, 344 pp.

McCoy, V.E., Young, R.T., Briggs, D.E. 2015. Factors controlling exceptional preservation in concretions. Palaios, 30(4): 272–280.

Myers, J.M., Antholine, W.E., Myers, C.R., 2004. Vanadium (V) reduction by *Shewanella oneidensis* MR-1 requires menaquinone and cytochromes from the cytoplasmic and outer membranes. Applied and Environmental Microbiology, 70(3): 1405–1412.

Middleton, G.V. 1960. Chemical composition of sandstones. Bulletin of the Geological Society of America, 71: 1011–1026. https://doi.org/10.1130/0016-7606(1960)71[1011:CCOS]2.0.CO;2

Naylor, H., Turner, P., Vaughan, D.J., Boyce, A.J., Fallick, A.E. 1989. Genetic studies of red-bed mineralization in the Triassic of the Cheshire basin, northwest England. Journal of the Geological Society, London, 146: 685–699.

Olsen, P.E., Kent, D.V., 1996. Milankovitch climate forcing in the tropics of Pangaea during the Late Triassic. Palaeogeography, Palaeoclimatology, Palaeoecology, 122: 1–26.

Panhuys-Sigler, V.M., Trewin, N.H., Still, J. 1996. Roscoelite associated with reduction spots in Devonian red beds, Gamrie Bay, Banffshire. Scottish Journal of Geology, 32: 127–132. https://doi.org/10.1144/sjg32020127.

Parnell, J., 1985, Uranium/rare earth-enriched hydrocarbons in Devonian sandstones, northern Scotland. Neues Jahrbuch fur Mineralogie, Monatshefte, 3: 132–144

Parnell, J., 1988. The mineralogy of red bed uranium-vanadium mineralization in the Permo-Triassic of Belfast. Irish Journal of Earth Sciences, 9: 119–124. https://www.jstor.org/stable/30002478

Parnell, J., Eakin, P., 1987, The replacement of sandstones by uraniferous hydrocarbons: significance for petroleum migration. Mineralogical Magazine, 51(4): 505–515. https://doi.org/10.1180/minmag.1987.051.362.05

Parnell, J., Spinks S., Bellis, D., 2016. Low-temperature concentration of tellurium and gold in continental red bed successions. Terra Nova, 28(3): 221–227. https://doi.org/10.1111/ter.12213.

Parnell, J., Spinks, S., Brolly, C., 2018. Tellurium and selenium in Mesoproterozoic red beds. Precambrian Research, 305: 145–150.

https://doi.org/10.1016/j.precamres.2017.12.022.

Pollastro, R.M., 1993. Considerations and applications of the illite/smectite geothermometer in hydrocarbon-bearing rocks of Miocene to Mississippian age. Clays and Clay Minerals, 41(2): 119–133.

Pytte, A.M., and R.C. Reynolds. 1989. "The thermal transformation of smectite to illite." *Thermal history of sedimentary basins*. Springer, New York, NY, 133-140.

Raiswell, R., Fisher, Q.J. 2000. Mudrock-hosted carbonate concretions: a review of growth mechanisms and their influence on chemical and isotopic composition. Journal of the Geological Society, 157(1): 239–251.

Rasmussen, B., Muhling, J.R., 2019. Syn-tectonic hematite growth in Paleoproterozoic Stirling Range “red beds”, Albany-Fraser Orogen, Australia: Evidence for oxidation during late-stage orogenic uplift. Precambrian Research, 321: 54–63. https://doi.org/10.1016/j.precamres.2018.12.002.

Retallack, G.J., 2008. *Soils of the past: an introduction to paleopedology*. John Wiley and Sons.

Rose, A.W., 1976. The effect of cuprous chloride complexes in the origin of red-bed copper and related deposits. Economic Geology, 71: 1036–1048. https://doi.org/10.2113/gsecongeo.71.6.1036

Rose, A.W., Bianchi-Mosquera, G.C., 1993. Adsorption of Cu, Pb, Zn, Co, Ni, and Ag on goethite and hematite; a control on metal mobilization from red beds into stratiform copper deposits. Economic Geology, 88(5): 1226–1236. https://doi.org/10.2113/gsecongeo.88.5.1226

Roser, B.P., Korsch, R.J. 1986. Determination of tectonic setting of sandstone-mudstone suites using SiO_2 content and K_2O/Na_2O ratio. Journal of Geology, 94: 635–650.

Sagemann, J., Bale, S.J., Briggs, D.E., Parkes, R.J. 1999. Controls on the formation of authigenic minerals in association with decaying organic matter: an experimental approach. Geochimica et Cosmochimica Acta, 63(7–8): 1083–1095.

Scott, A.C. 2010. Charcoal recognition, taphonomy and uses in palaeoenvironmental analysis. Palaeogeography, Palaeoclimatology, Palaeoecology, 291: 11–39.

Shawe, D.R., 2011. Uranium-vanadium deposits of the Slick Rock district, Colorado. United States Geological Survey, Professional Paper, 576: 1–80.

Shen, W., Liu, S., Zhang, B., Wang, Y., Wang, Z., Fang, M., Li, X., 2020. Cretaceous tectonic evolution of Jiaolai basin. Geotectonics and Metallogeny, 44(03): 325–339 (in Chinese with English language summary).

Sherlock, R.L., 1947. *The Permo-Triassic Formations. A World Review*. Hutchinson, Scientific and Technical Publications, London, 367pp.

Spinks, S.C., Parnel, J., Bowden, S.A. 2010. Reduction spots in the Mesoproterozoic age: Implications for life in the early terrestrial record. International Journal of Astrobiology, 9: 209–216. https://doi.org/10.1017/S1473550410000273.

Spinks, S.C. 2012. Geological evidence for the oxygenation of the atmosphere in the Torridonian, and contemporaneous successions. PhD Thesis, University of Aberdeen Library, Entry 001497336.

Spinks, S.C., Parnel, J., Still, J.W. 2014. Redox-controlled selenide mineralization in the Upper Old Red Sandstone. Scottish Journal of Geology, 50 (2): 173–182. https://doi.org/10.1144/sjg2013-014.

Su, C., Zhang, M., Lin, L., Yu, G., Zhong, H., Chong, Y., 2020. Reduction of iron oxides and microbial community composition in iron-rich soils with different organic carbon as electron donors. International Biodeterioration and Biodegradation, 148: Art. 104881. https://doi.org/10.1016/j.ibiod.2019.104881

Suttner, L.J., Dutta, P.K., 1986. Alluvial sandstone composition and paleoclimate; I, Framework mineralogy. Journal of Sedimentary Research, 56(3): 329–345.

Thorson, J.P., 2004. Paradox Basin sandstone-hosted copper deposits generated by two episodes of basinal fluid expulsion. Geological Society of America, Abstracts with Programs, 36(5): 517.

Tian, J., Chen J., Lu H., Chen, C., Wang, H., Li, T., Li, S., Wang, Q., Zhang, H., Wan, X., 2021. Discovery of charophyte flora across the Cretaceous–Paleocene transition in the Jiaolai Basin. Palaeoworld, 30(3): 538–550. https://doi.org/10.1016/j.palwor.2020.09.007

Tian, J., Zhang, X., 2016. *Sedimentary geochemistry*. Chinese book of Geological Publishing House, Beijing, ISBN: 9787116096462, 21–83 (in Chinese language).

Trendell, A.M., Nordt, L.C., Atchley, S.C., Leblanc, S.L., Dworkin, S.I., 2013. Determining floodplain plant distributions and populations using paleopedology and fossil root traces: Upper Triassic Sonsela Member of the Chinle Formation at Petrified Forest National Park, Arizona. Palaios, 28(7): 471–490. https://doi.org/10.2110/palo.2012.p12-065r

Turner, P. 1980. Continental Red Beds. Developments in Sedimentology, 29: 1–562. Elsevier.

Tyson, R.V., 1995. Sedimentary Organic Matter: Organic facies and palynofacies. Chapman and Hall. 591 pgs.

Van Houten, F.B., 1973. Origin of red beds a review: 1961-1972. Annual Review of Earth and Planetary Sciences, 1(1): 39–61. https://doi.org/10.1146/annurev.ea.01.050173.000351

Walker, T.R., 1967. Formation of red beds in modern and ancient deserts. Geological Society of America Bulletin, 78(3): 353–368. https://doi.org/10.1130/0016-7606(1968)79[281:FORBIM]2.0.CO;2

Walker, T.R., 1974. Formation of red beds in moist tropical climates: a hypothesis. Geological Society of America Bulletin, 85(4): 633–638. https://doi.org/10.1130/0016-7606(1974)85<633:FORBIM>2.0.CO;2

Walker, T.R., 1976. Diagenetic origin of continental red beds. In: The Continental Permian in Central, West, and South Europe (pp. 240–282). Springer, Dordrecht.

Walker, T.R., Waugh, B., Crone, A.J. 1978. Diagenesis in first-cycle desert alluvium of Cenozoic age, southwestern United States and northwestern Mexico. Geological Society of America Bulletin, 89(1): 19–32.

Wang, H., Li, S., Zhang, H.C., Cao, M., Horne, D.J., 2019. Biostratigraphic and palaeoenvironmental significance of Campanian-early Maastrichtian (Late Cretaceous) ostracods from the Jiaozhou Formation of Zhucheng, Shandong, China. Cretaceous Research, 93: 4–21.

https://doi.org/10.1016/j.cretres.2018.08.023.

Xu, K., Kuang, H., Qin, J., Wang, Y., Peng, N., Ning, Z., Zhang, F., Liu, Y., 2017. New discovery of terrestrial K-Pg boundary from Jiaolai Basin of Shandong Province, 44(1): 194–195 (in Chinese with English language summary).

Yang, Y., Fu, W., Yu, J., Ning, Z., Cui, J., Li, Q., Wang, X., Zhou, X. 2019. Formation mechanism of reduction spheroids with dark cores in Cretaceous red beds in Jiaolai Basin, China. Open Journal of Geology 9: 707–710. doi: 10.4236/ojg.2019.910081.

Yang, Y., Fu, W., Yu, J., Ning, Z., Cui., J. Li, Q., Zhou, X., Chen, J. 2021. Cyclostratigraphical analysis of continental red beds below K/Pg boundary in the Jiaolai Basin. Acta Sedimentological Sinica, 39(4): 942–952 (in Chinese with English Abstract).

Yu, T., Salvador, R.B., Wang, H., Fang, Y., Neubauer, T. A., Li, S., Zhang, H., Wan, X., 2021. A latest Cretaceous gastropod fauna from the Jiaolai Basin of East Asia, Cretaceous Research, 121: 1–8. https://doi.org/10.1016/j.cretres.2020.104736

Zhang, Y., Dong, S., Shi, W., 2003. Cretaceous deformation history of the middle Tan-Lu fault zone in Shandong Province, eastern China. Tectonophysics, 363: 243–258 (in Chinese with English language summary).

Zhang, B., Liu, S.F., Lin, C.F., Wang, Y., Wang, Z.H., Fang, M., Shen, W.J. 2021. Provenance of the Late Cretaceous sediments in Jiaolai Basin, Eastern China, and its tectonic implications. International Geology Review, 63(8): 973–991 https://doi.org/10.1080/00206814.2020.1737840

Figure captions

Figure 1. Location maps showing position and the Jiaolai Basin. **A**, Map of northeast China, Mongolia and Russia. **B**, Enlargement of boxed area from A showing major tectonic units in northeast China. **C**, Enlargement of boxed area from B showing the Jiaolai Basin and position of the studied boreholes (modified from Han et al., 2020).

Figure 2. Correlated sedimentary logs from the JK-1 and L-K1 boreholes in the Jiaolai Basin showing lithostratigraphy, Gamma Ray (GR) log, cyclostratigraphy based on GR values, sedimentary facies and faunal distributions; charophyte and gastropod ranges from the LK-1 borehole based on Yu (2021). M - Mudstone; SM - Silty Mudstone; AS - Argillaceous Siltstone; Sil - Siltstone; Sst - Sandstone; Cg/Ba - Conglomerate or Basalt

Figure 3. Example reduction spots and fossils on bedding planes of the JK-1 borehole in the Jiaolai Basin. **A**, Small spheroidal reduction spot with sharp boundary containing occasional flecks of red sediment. **B**, Small spheroidal reduction spot near a larger reduction spot each. **C**, Dark red sedimentary matrix with longitudinally elongate reduction spots surrounding elongate loci that comprise fossil plant roots oriented parallel to bedding. **D–F**, Variations in irregular reduction spot morphology cross-cutting bedding and with occasional red inclusions. **G**, Elongate, tubular reduction spots with thin, tubular cores oriented vertically and near-vertically in the

sediment most likely representing palaeosol roots. **H**, Reduction spots in vertically split core showing intricate and irregular nature that cross-cuts bedding. **I**, Bedding plane showing large, tubular reduction spot with elongated black locus, and several smaller, isolated, spheroidal reduction spots. **J**, Enlargement from **3I** showing sharp reduction spot margin with adjacent white gypsum crystal and isolated, black, refractory fossil charcoal fragment that each lack enveloping reduction spots.

Figure 4. Reduction spots characteristics. **A**, Distribution of diameters with the lithology; **B**, Distribution of diameters with the shape of reduction spots; **C**, Distribution of diameters with the cores contained in reduction spots; **D**, Distribution of diameters with the different boundary between reduction spots and red beds;

Figure 5. Details of the boundary between reduction spots and host sediment. **A**. Stereoscope image showing the clear boundary between the reduction spot and surrounding host red sediment. **B**. Thin section photomicroscope illustrating the differences in opaque and pigmentary iron oxide content between host red sediment and reduction spot. Opaque specularite grains with pigmentary grain coatings are abundant in the red host sediment. Specualrite grains are less abundant and much smaller in the reduction spot area**. C.** Detailed thin section photomicroscope illustrating the sharp boundary (dashed yellow line) of the red sediments with abundant pigmentary hematite coating grains and the reduction spot with no pigmentary hematite.

Figure 6. Elemental composition of reduction spot and surrounding sediments. **A,** Major element content of samples in JK-1 borehole; **B**, Trace element content of samples in JK-1 borehole; **C**, Major elements in from sediment and reduction spots in the JK-1 borehole showing overall similar compositions. **D**, Trace element composition from the JK-1 borehole showing elevated Vanadium (V) and Barium (Ba) and depleted Cadmium (Cd) concentrations. **E**, Trace element composition in the JK1 borehole compared with reduction spots from Colorado (Hofmann, 1991) that also show elevated Vanadium (V) but at significantly higher concentrations.

Figure 7. A, K_2O/Na_2O-SiO_2/Al_2O_3 diagram plotting samples from the JK-1 borehole (empty circles) against lithologies typical of continental island arcs (I), oceanic island arcs (II), active continental margin (III) and passive continental margin (IV). **B**, La-Th-Sc discrimination diagram plotting samples from the JK-1 borehole (cope circles) with sediments from passive continental margins (A), sediments related to magmatic arcs (B), ocean island alkaline basalt (C), and shale sediments in post-Archean Australia (D) (modified from Mao and Liu, 2011; Tian and Zhang, 2016).

Figure 8. Whole rock X-ray diffraction analysis results of samples from red host rocks compared with a green reduction spot. Harmotome and maghemite are largely absent in the green reduction spot and there is a notable reduction in the amount of montmorillonite. The results are consistent with those from the XCT.

Figure 9. 3D X-ray Computed Tomography (XCT) analysis of sample *zk06g* showing relative density differences in the sample. Three views are shown, each rotated in a vertical plane ~45 degrees apart in a clockwise direction from left to right (e.g., D to E to F; white arrows represent the same features across views). Each view has three corresponding but distinct data visualizations (View 1 = A, D, G; View 2 = B, E, H; View 3 = C, F, I). First visualisation **A, B, C** shows the surface rending of the CT data after converting and stretching to the 8-bit pixel range (corresponding grayscale scale given on right). The second **D, E, F** shows the false colour volume rendering based of the raw unaltered 16-bit CT data (corresponding colour scale given on right). The third **G, H, I** shows a combination of the previous two visualisations, overlaying the false colour data on the 3D geometry of the sample. In all views the boundary of the reduction spot and red sediment can be readily distinguished (dotted line) and is most clearly delimited in false colour images in which the reduction spot has a lower relative density (blue), contains fewer high relative density (red) features, and the contains fewer and smaller mid-high relative density orange features. The specimen does not contain the center of the reduction spot to identify the core but contains a large, rhomboidal, relative mid-density (yellow orange) crystal (labeled as X, in C, F, and I). This is particularly apparent in false colour image (F) were it stands out from the low-density background of the reduction spot. This method does not permit the density to be quantified in absolute nor the composition of the different density materials to be identified. Note that the 1cm scale bar (bottom right) is an indication

of scale in the foreground only due to the orthographic projection of 3D data onto a 3D plane.

Figure 10. Back scattered electron (BSE) analyses of reduction spots and black core from the sample zk06g. A. P17, P18 and P19 located in the green reduction spot. B. P7, P10, P11in the black core area. C, D, E show analyses for the green reduction spot with the presence of vanadium. **D, E, F** show analyses from the black core area showing the absence of vanadium

Figure 11. Model for the formation of reduction spots in Cretaceous red beds in the Jiaolai Basin, China. Abbreviations: Eh=+ve = positive activity of electrons; VO = Vanadium oxide.

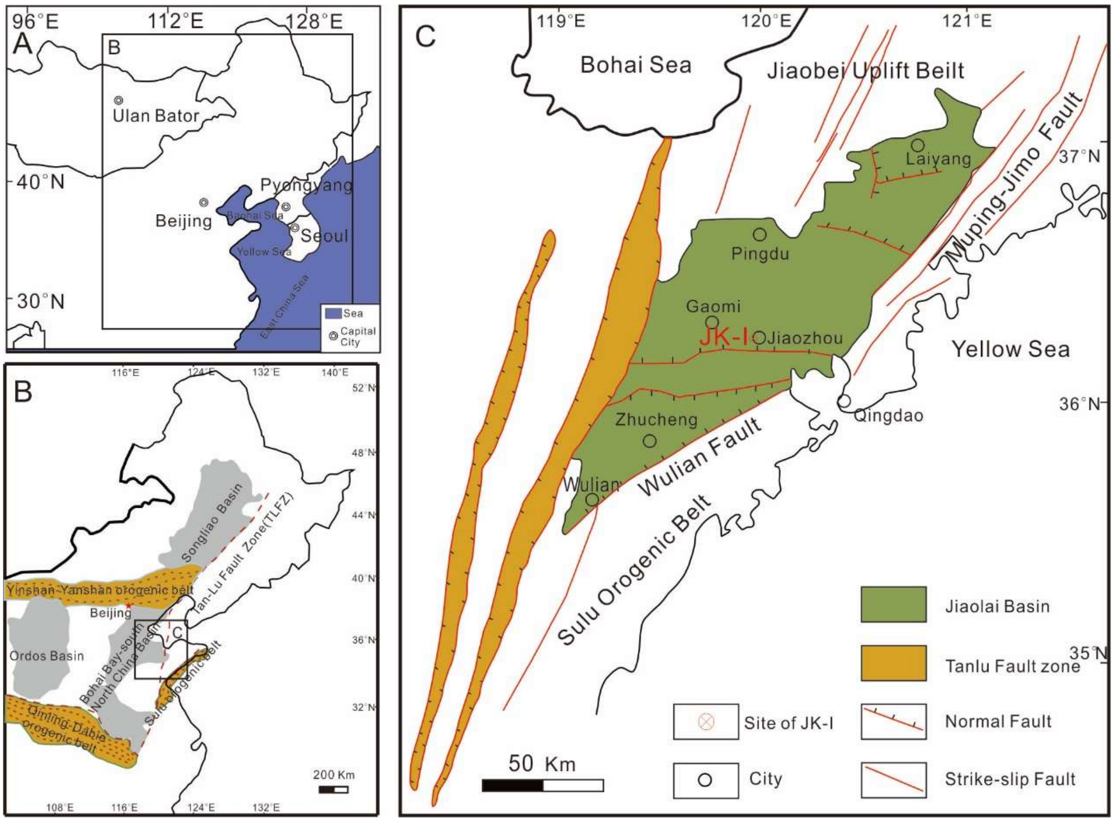

96°E
112°E
128°E
A
B
Ulan Bator
40°N
Pyongyang
Beijing
Seoul
Yellow Sea
30°N
East China Sea
Sea
Capital City
B
116°E
124°E
132°E
140°E
52°N
48°N
44°N
40°N
36°N
32°N
Songliao Basin
Tan-Lu Fault Zone(TLFZ)
Yinshan-Yanshan orogenic belt
Beijing
Ordos Basin
Bohai Bay-south North China Basin
C
Sulu orogenic belt
Qinling-Dabie orogenic belt
200 Km
108°E
116°E
124°E
132°E
C
119°E
120°E
121°E
Bohai Sea
Jiaobei Uplift Beilt
Laiyang
37°N
Muping-Jimo Fault
Pingdu
Gaomi
JK-I
Jiaozhou
Yellow Sea
36°N
Qingdao
Zhucheng
Wulian Fault
Wulian
Sulu Orogenic Belt
Jiaolai Basin
Tanlu Fault zone
35°N
Site of JK-I
Normal Fault
50 Km
City
Strike-slip Fault

Figure 1

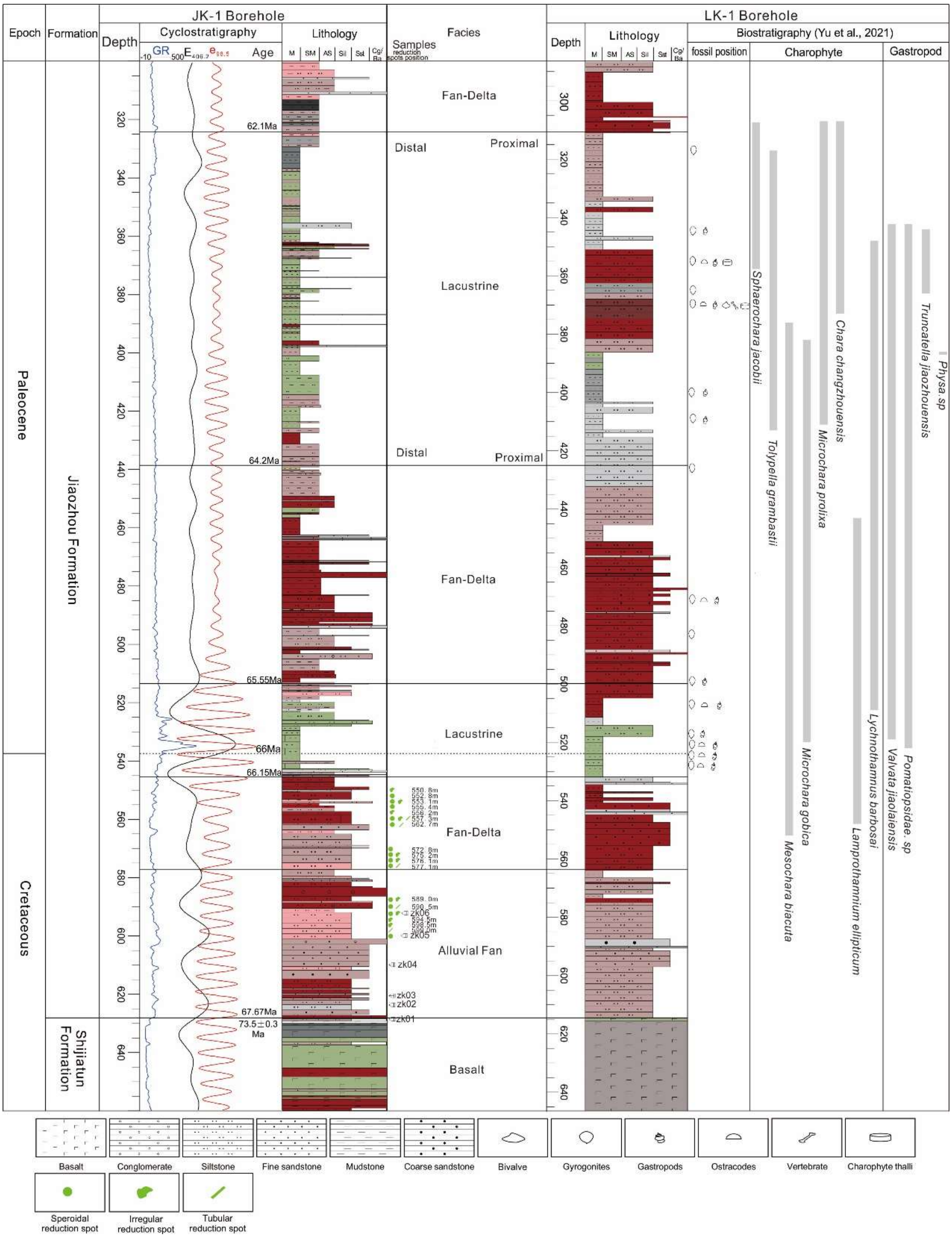

JK-1 Borehole
LK-1 Borehole
Epoch
Formation
Depth
Cyclostratigraphy
Lithology
Age
Samples
Facies
Biostratigraphy (Yu et al., 2021)
fossil position
Charophyte
Gastropod
Paleocene
Cretaceous
Jiaozhou Formation
Shijiatun Formation
Fan-Delta
Distal
Proximal
Lacustrine
Alluvial Fan
Basalt
62.1Ma
64.2Ma
65.55Ma
66Ma
66.15Ma
67.67Ma
73.5±0.3 Ma
Sphaerochara jacobi
Tolypella grambastii
Mesochara biacuta
Microchara gobica
Microchara prolixa
Chara changzhouensis
Lamprothamnium ellipticum
Lychnothamnus barbosai
Valvata jiaolaiensis
Pomatiopsidae. sp
Truncatella jiaozhouensis
Physa sp
Basalt
Conglomerate
Siltstone
Fine sandstone
Mudstone
Coarse sandstone
Bivalve
Gyrogonites
Gastropods
Ostracodes
Vertebrate
Charophyte thalli
Speroidal reduction spot
Irregular reduction spot
Tubular reduction spot

Figure2

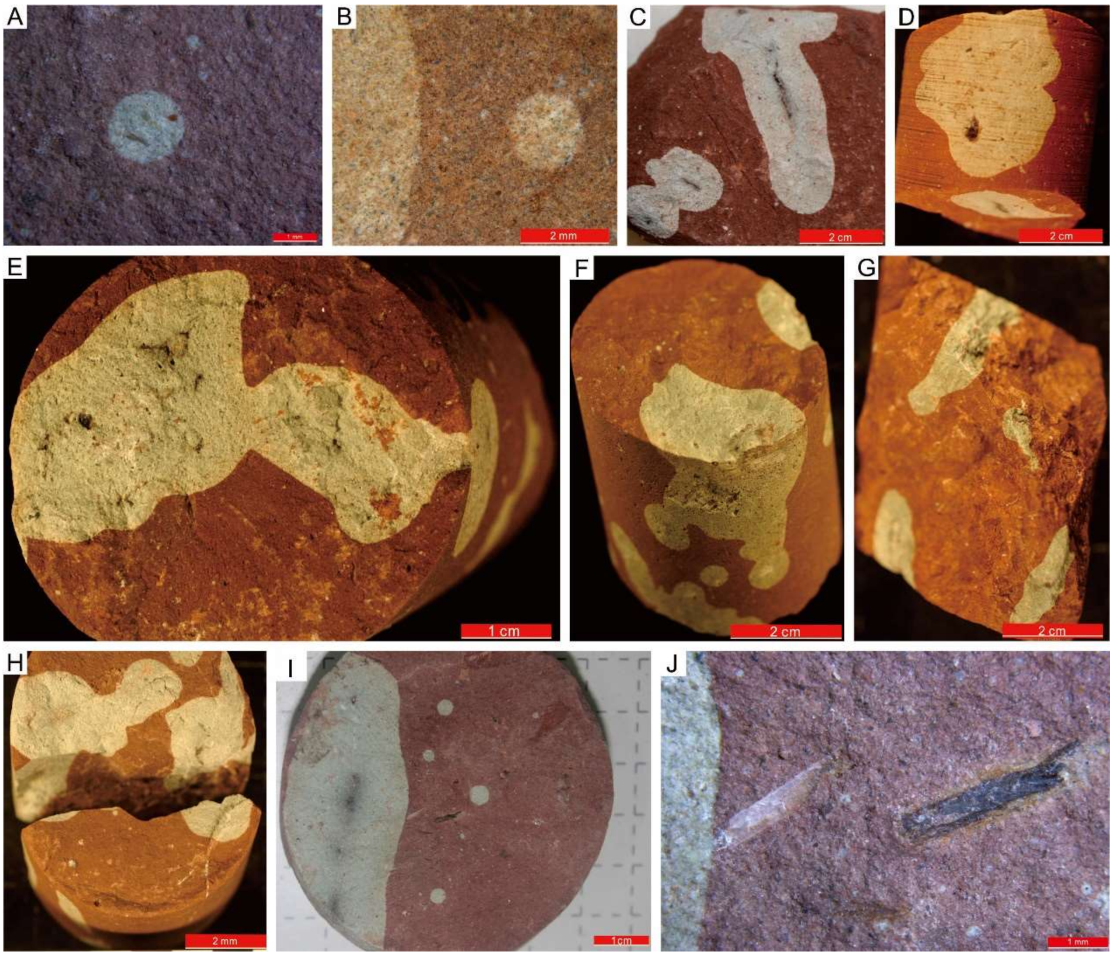

Figure 3

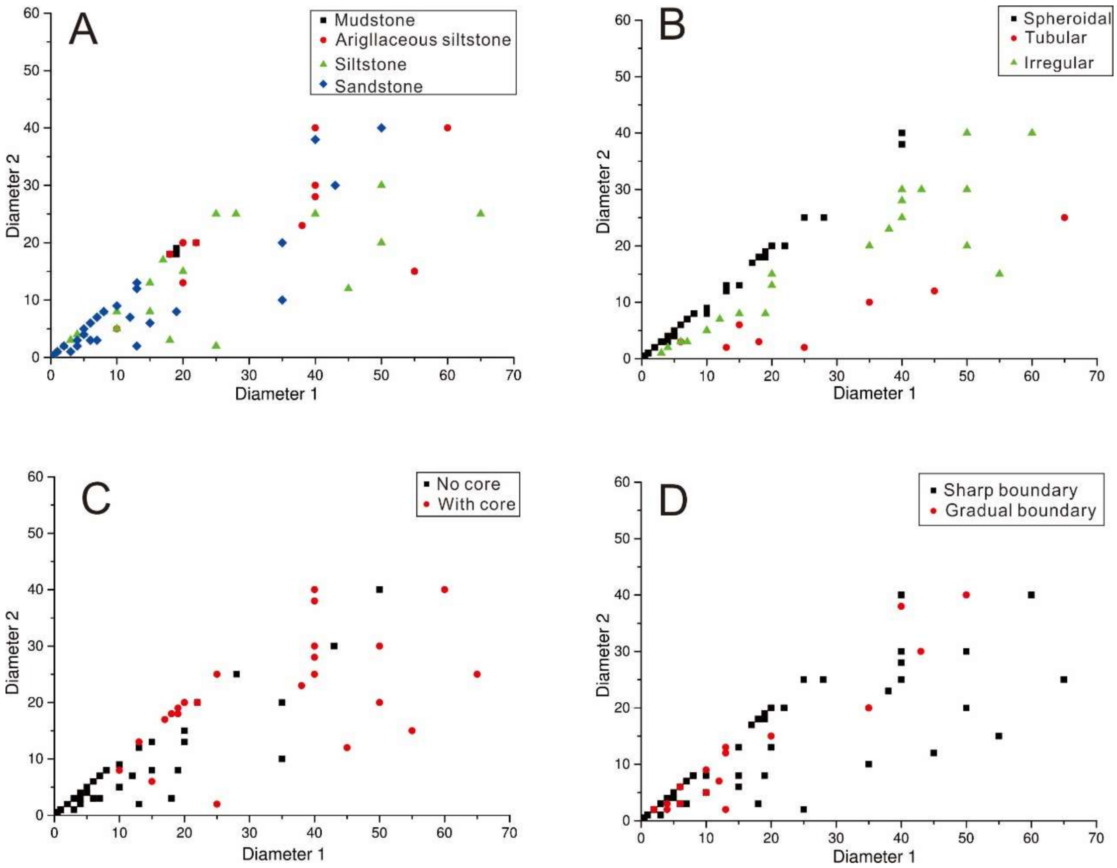
A
Mudstone
Arigllaceous siltstone
Siltstone
Sandstone
Diameter 1
Diameter 2
B
Spheroidal
Tubular
Irregular
C
No core
With core
D
Sharp boundary
Gradual boundary

Figure 4

1153

1154 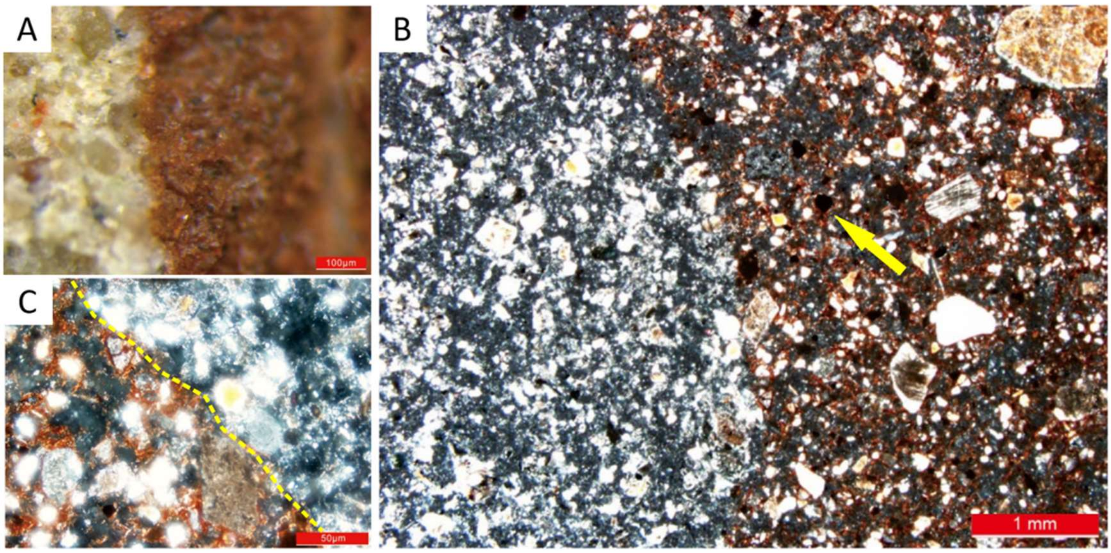

1155 Figure 5

1156

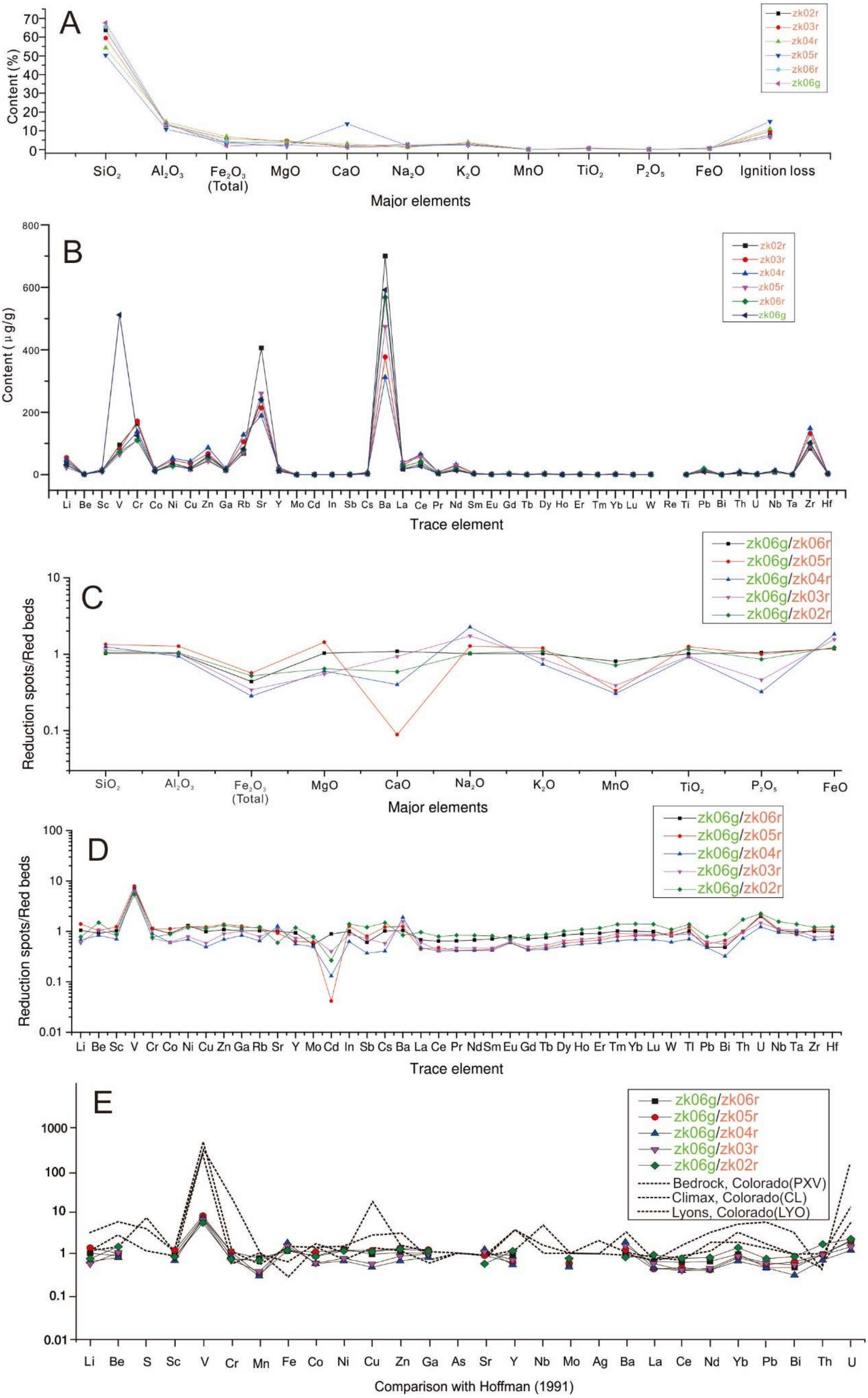
A
Content (%)
zk02r
zk03r
zk04r
zk05r
zk06r
zk06g
SiO2 Al2O3 Fe2O3 (Total) MgO CaO Na2O K2O MnO TiO2 P2O5 FeO Ignition loss
Major elements
B
Content (μ g/g)
Li Be Sc V Cr Co Ni Cu Zn Ga Rb Sr Y Mo Cd In Sb Cs Ba La Ce Pr Nd Sm Eu Gd Tb Dy Ho Er Tm Yb Lu W Re Ti Pb Bi Th U Nb Ta Zr Hf
Trace element
C
Reduction spots/Red beds
zk06g/zk06r
zk06g/zk05r
zk06g/zk04r
zk06g/zk03r
zk06g/zk02r
SiO2 Al2O3 Fe2O3 (Total) MgO CaO Na2O K2O MnO TiO2 P2O5 FeO
Major elements
D
Reduction spots/Red beds
Li Be Sc V Cr Co Ni Cu Zn Ga Rb Sr Y Mo Cd In Sb Cs Ba La Ce Pr Nd Sm Eu Gd Tb Dy Ho Er Tm Yb Lu W Tl Pb Bi Th U Nb Ta Zr Hf
Trace element
E
Bedrock, Colorado(PXV)
Climax, Colorado(CL)
Lyons, Colorado(LYO)
Li Be S Sc V Cr Mn Fe Co Ni Cu Zn Ga As Sr Y Nb Mo Ag Ba La Ce Nd Yb Pb Bi Th U
Comparison with Hoffman (1991)

Figure 6

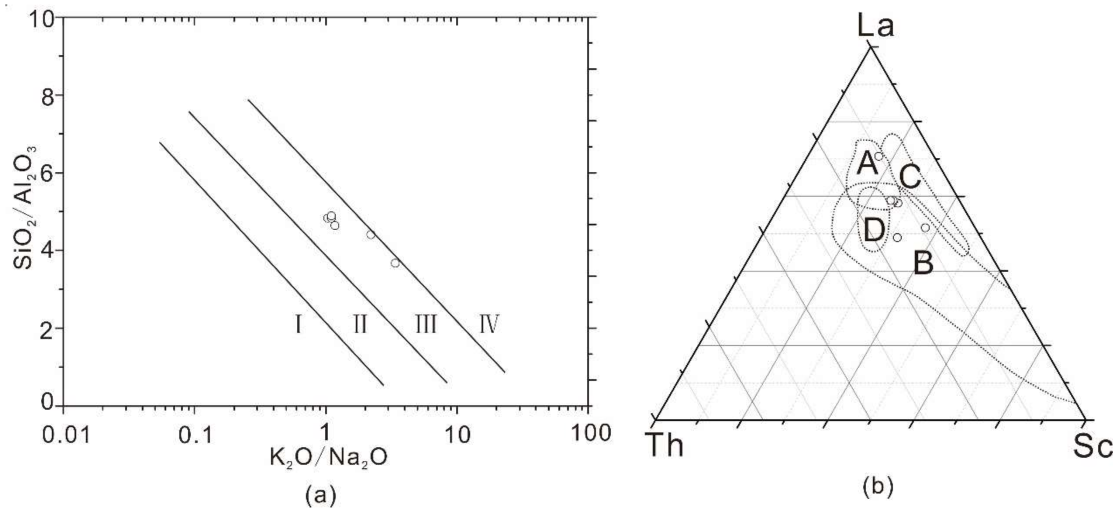
SiO2/Al2O3
K2O/Na2O
0.01
0.1
1
10
100
0
2
4
6
8
10
I
II
III
IV
(a)
La
Th
Sc
A
B
C
D
(b)

Figure 7

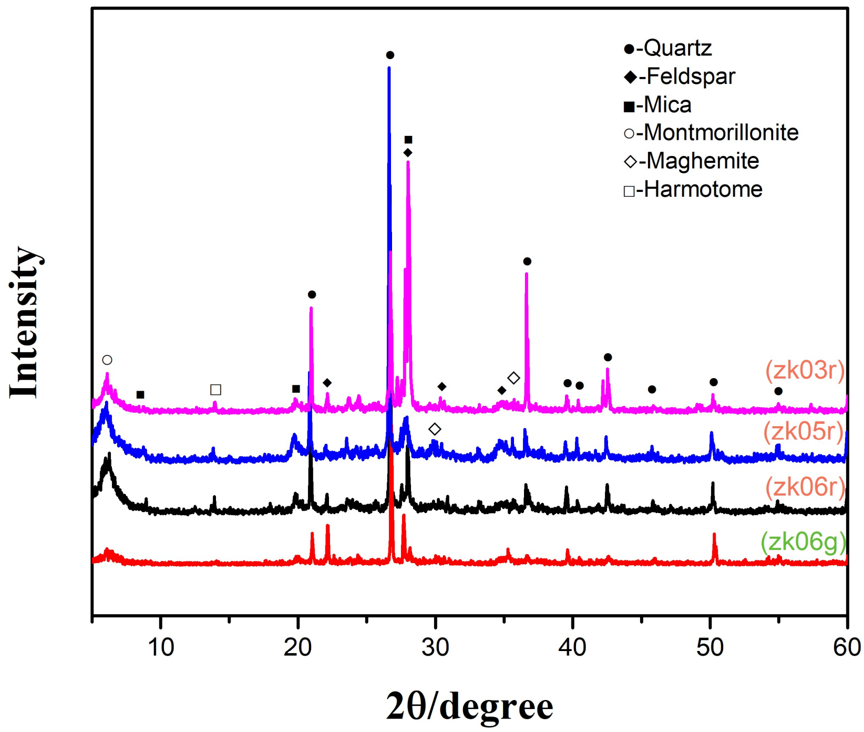
●-Quartz
◆-Feldspar
■-Mica
○-Montmorillonite
◇-Maghemite
□-Harmotome
(zk03r)
(zk05r)
(zk06r)
(zk06g)
Intensity
10
20
30
40
50
60
2θ/degree

Figure 8

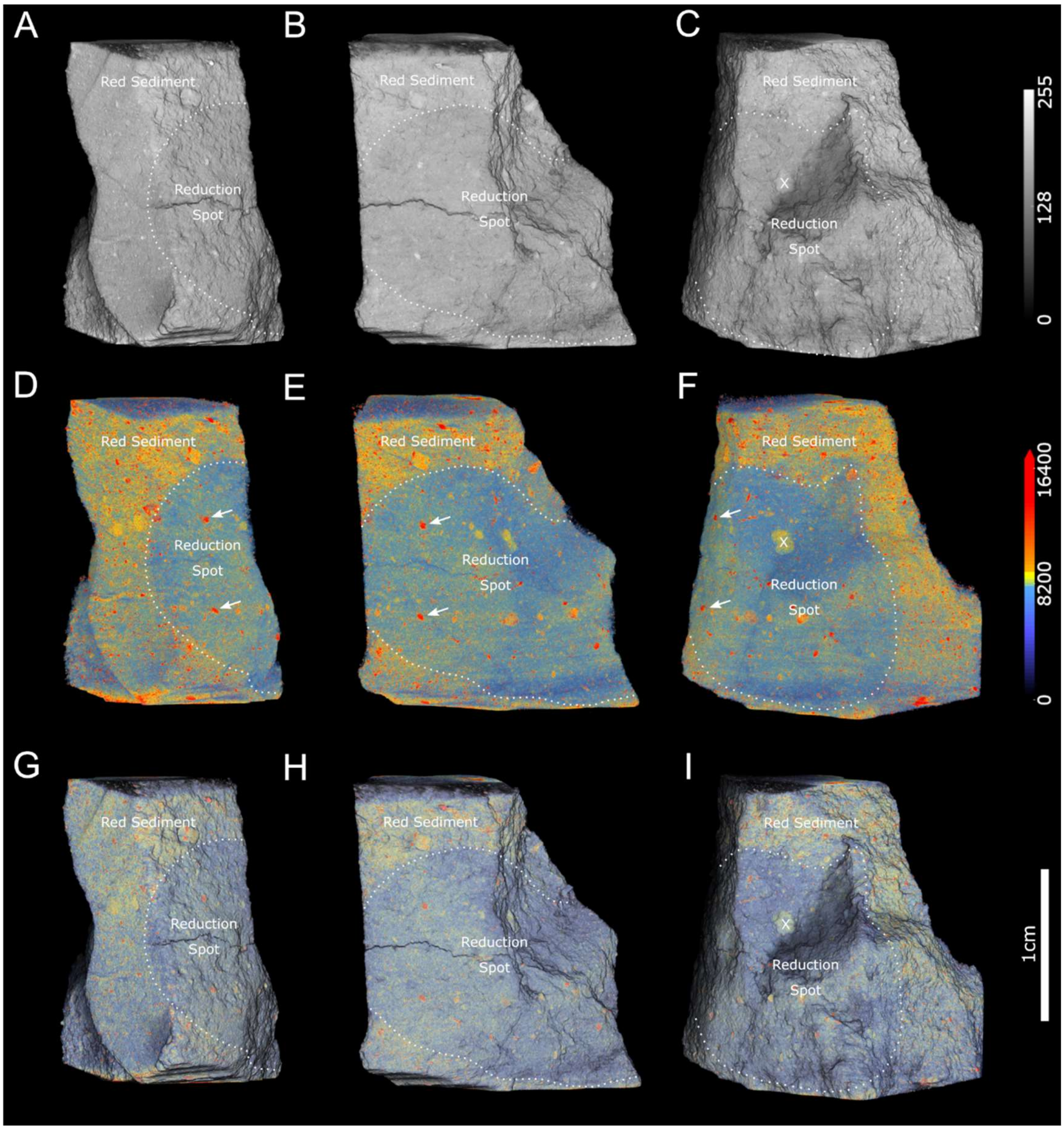
A
B
C
D
E
F
G
H
I
Red Sediment
Reduction Spot
X
255
128
0
16400
8200
0
1cm

Figure 9

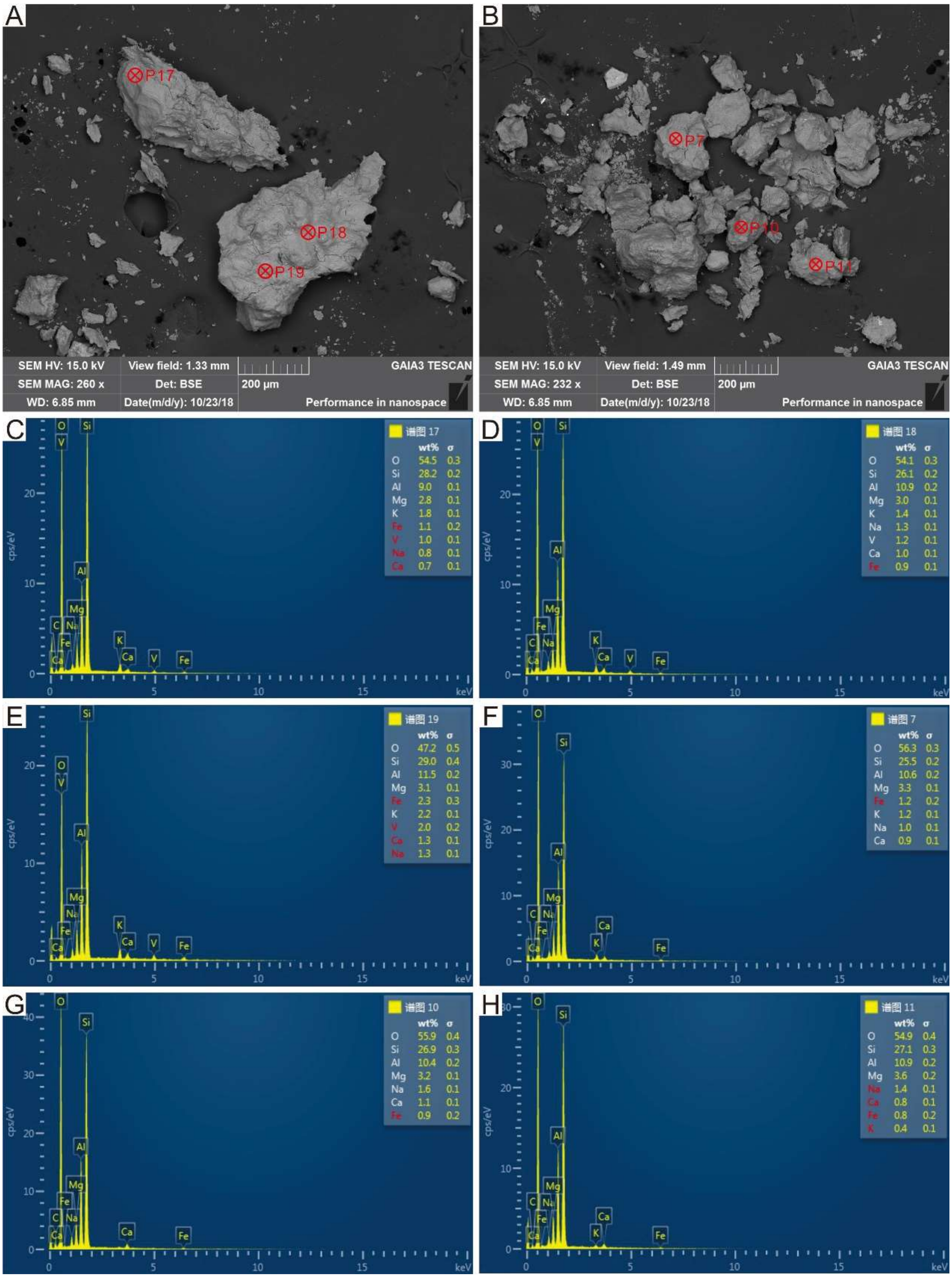
A
P17
P18
P19
SEM HV: 15.0 kV
View field: 1.33 mm
GAIA3 TESCAN
SEM MAG: 260 x
Det: BSE
200 µm
WD: 6.85 mm
Date(m/d/y): 10/23/18
Performance in nanospace
B
P7
P10
P11
SEM HV: 15.0 kV
View field: 1.49 mm
GAIA3 TESCAN
SEM MAG: 232 x
Det: BSE
200 µm
WD: 6.85 mm
Date(m/d/y): 10/23/18
Performance in nanospace
C
谱图 17
wt% σ
O 54.5 0.3
Si 28.2 0.2
Al 9.0 0.1
Mg 2.8 0.1
K 1.8 0.1
Fe 1.1 0.2
V 1.0 0.1
Na 0.8 0.1
Ca 0.7 0.1
D
谱图 18
wt% σ
O 54.1 0.3
Si 26.1 0.2
Al 10.9 0.2
Mg 3.0 0.1
K 1.4 0.1
Na 1.3 0.1
V 1.2 0.1
Ca 1.0 0.1
Fe 0.9 0.1
E
谱图 19
wt% σ
O 47.2 0.5
Si 29.0 0.4
Al 11.5 0.2
Mg 3.1 0.1
Fe 2.3 0.3
K 2.2 0.1
V 2.0 0.2
Ca 1.3 0.1
Na 1.3 0.1
F
谱图 7
wt% σ
O 56.3 0.3
Si 25.5 0.2
Al 10.6 0.2
Mg 3.3 0.1
Fe 1.2 0.2
K 1.2 0.1
Na 1.0 0.1
Ca 0.9 0.1
G
谱图 10
wt% σ
O 55.9 0.4
Si 26.9 0.3
Al 10.4 0.2
Mg 3.2 0.1
Na 1.6 0.1
Ca 1.1 0.1
Fe 0.9 0.2
H
谱图 11
wt% σ
O 54.9 0.4
Si 27.1 0.3
Al 10.9 0.2
Mg 3.6 0.2
Na 1.4 0.1
Ca 0.8 0.1
Fe 0.8 0.2
K 0.4 0.1
cps/eV
keV

Figure 10

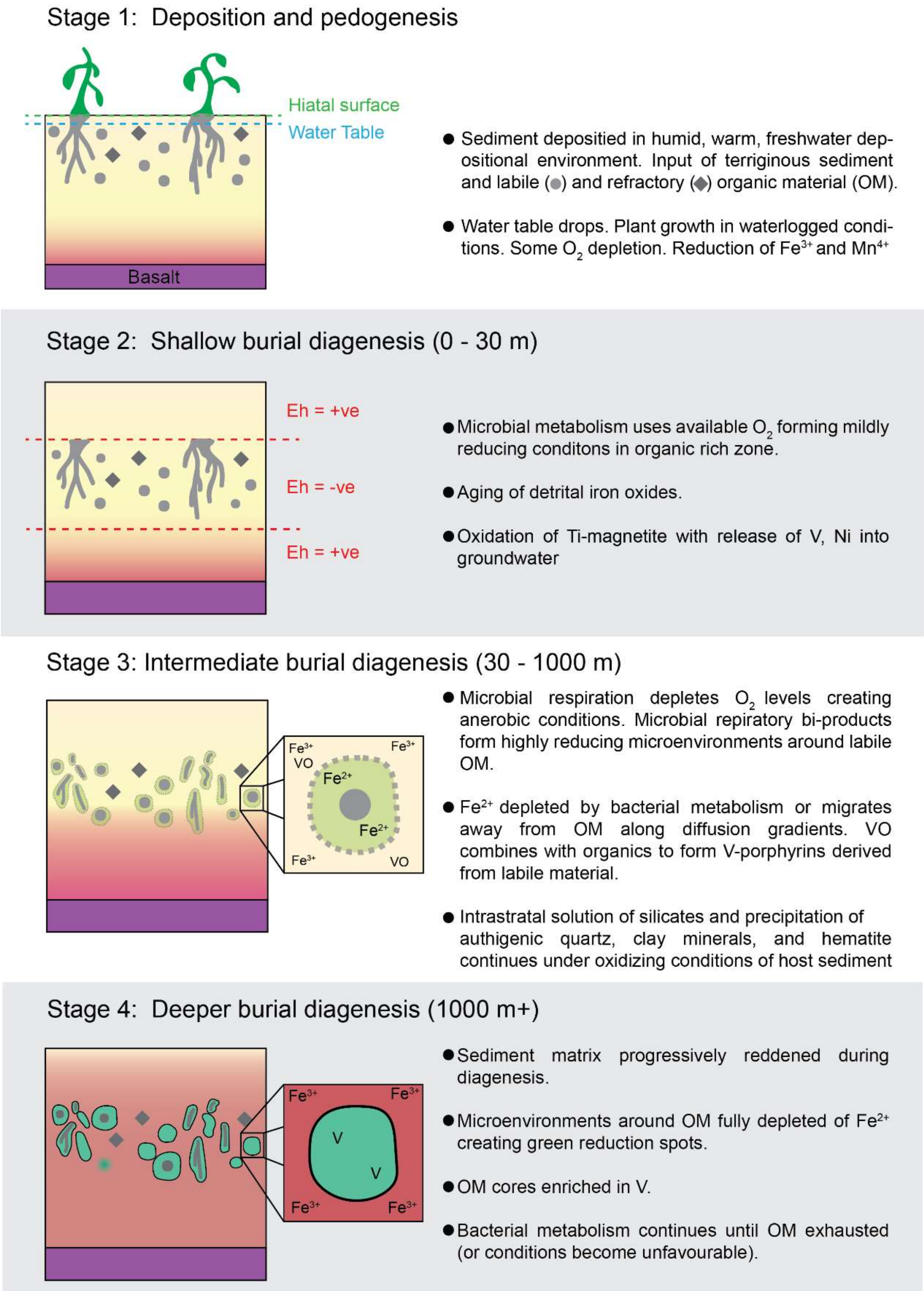

Stage 1: Deposition and pedogenesis
Hiatal surface
Water Table
Basalt
Sediment depositied in humid, warm, freshwater depositional environment. Input of terriginous sediment and labile (●) and refractory (◆) organic material (OM).
Water table drops. Plant growth in waterlogged conditions. Some O_2 depletion. Reduction of Fe^{3+} and Mn^{4+}
Stage 2: Shallow burial diagenesis (0 - 30 m)
Eh = +ve
Eh = -ve
Eh = +ve
Microbial metabolism uses available O_2 forming mildly reducing conditons in organic rich zone.
Aging of detrital iron oxides.
Oxidation of Ti-magnetite with release of V, Ni into groundwater
Stage 3: Intermediate burial diagenesis (30 - 1000 m)
Fe^{3+}
VO
Fe^{2+}
Fe^{3+}
Fe^{2+}
Fe^{3+}
VO
Microbial respiration depletes O_2 levels creating anerobic conditions. Microbial repiratory bi-products form highly reducing microenvironments around labile OM.
Fe^{2+} depleted by bacterial metabolism or migrates away from OM along diffusion gradients. VO combines with organics to form V-porphyrins derived from labile material.
Intrastratal solution of silicates and precipitation of authigenic quartz, clay minerals, and hematite continues under oxidizing conditions of host sediment
Stage 4: Deeper burial diagenesis (1000 m+)
Fe^{3+}
Fe^{3+}
V
V
Fe^{3+}
Fe^{3+}
Sediment matrix progressively reddened during diagenesis.
Microenvironments around OM fully depleted of Fe^{2+} creating green reduction spots.
OM cores enriched in V.
Bacterial metabolism continues until OM exhausted (or conditions become unfavourable).

Figure 11